

## Full length article

# Numerical studies of gasoline direct-injection sprays (ECN Spray G) under early- and late-injection conditions using Large Eddy Simulation and droplets-statistics-based Eulerian–Lagrangian framework



Hao-Pin Lien <sup>a,\*</sup>, Yongxiang Li <sup>b</sup>, Andrea Pati <sup>a</sup>, Amsini Sadiki <sup>b</sup>, Christian Hasse <sup>a</sup>

<sup>a</sup> Technical University Darmstadt, Department of Mechanical Engineering, Simulation of reactive Thermo-Fluid Systems, Otto-Berndt-Str. 2, Darmstadt, 64287, Germany

<sup>b</sup> Technical University Darmstadt, Department of Mechanical Engineering, Reactive Flows and Diagnostics, Otto-Berndt-Str. 3, Darmstadt, 64287, Germany

## ARTICLE INFO

**Keywords:**

Engine Combustion Network (ECN)  
Spray G  
Constant-volume chamber  
Early-injection  
Late-injection  
Gasoline direct-injection  
Large Eddy Simulation

## ABSTRACT

This paper presents an approach that uses Large Eddy Simulation under the Eulerian–Lagrangian framework to model the gasoline direct-injection (GDI) spray from Engine Combustion Network (ECN) multi-hole and counter-bore injectors. The approach considers the significant role that cavitation plays in primary atomization due to the counter-bore configuration. The local Weber number (We) and Reynolds number (Re) for GDI sprays are much smaller than those for a diesel spray, which renders conventional diesel spray approaches unsuitable. The proposed one uses a statistics-based droplet distribution function to address this and incorporates necessary information from a DNS inner-nozzle flow simulation. The corresponding models for drag, heat transfer, evaporation, and breakup consider the effects of viscous and distorted spray droplets. The approach has been applied to two different operating conditions, with simulation results that agree well with experimental data. Compared to the blob method assuming the ejected droplets are at the size of the injector diameter, the proposed CFD framework can reproduce a more accurate plume shape in the Spray G3 case. Applying the late-injection condition (Spray G1), the proposed approach improves the projected liquid volume (PLV) extinction compared to the blob method by providing a more accurate droplet evaporation prediction. These findings demonstrate the significance of the proposed approach for modeling GDI sprays and highlight its potential for future research in this area.

## 1. Introduction

In recent decades, engineers and researchers have devoted themselves to reducing emissions and improving the performance of internal combustion engines (**ICES**). Both goals have been successfully achieved by reducing the size of spark-ignition (**SI**) engines and switching the injection system from port fuel injection (**PFI**) to **GDI**. Since 2020, half of all new vehicles and approximately 30 percent of SUV truck sales have featured gasoline direct-injection (**GDI**) engines [1]. This trend in the market shares is expected to be maintained by manufacturing more advanced **GDI** engines. Advanced GDI engines focus on improving the spray in-cylinder process, which involves spray, mixture formation, and combustion, to achieve homogeneous combustion and high fuel economy during high-load engine operation. Furthermore, during low-load engine operation, the spray-flow interaction is required to reach lean and ultra-lean stratified combustion without excessive unburned hydrocarbons and nitrogen oxides (NOx) [2]. This success requires a great understanding of the spray and in-cylinder flow interaction within

the **GDI** engines. Multi-hole injectors have been proven beneficial for the **GDI** engines due to their cost performance and the flexibility of nozzle design (hole- or swirl-type) and orientation [3]. Compared to diesel engine sprays, the multi-hole gasoline injectors operate under an approximately ten times lower injection pressure, 50 to 200 bar. The low injection pressure may result in insufficient atomization and consequently affect combustion due to low air entrainment and poor air-fuel mixing. One solution for that is often to apply low needle lifts shortening the overall injection and counter-bore inner nozzles, which yield a massive jet flow traveling through the internal nozzle and further generating compressible effects, such as cavitation and hydraulic flip. This feature of the gasoline spray, therefore, behaves differently from diesel sprays. Although there is an abundance of experimental and numerical research into diesel sprays, it cannot merely be applied to gasoline sprays.

The spray characteristics of **GDI** multi-hole injectors in either a constant-volume chamber or real direct-injection spark-ignition (**DISI**)

\* Corresponding author.

E-mail address: [lien@stfs.tu-darmstadt.de](mailto:lien@stfs.tu-darmstadt.de) (H.-P. Lien).

engines have been extensively studied [4–8]. However, the multi-hole injectors applied in each study differ in terms of their operating conditions and geometry, despite the consistency of the scientific discoveries. This occurrence yields difficulties in the validation of numerical modelings and experimental approaches. Such difficulties are advanced by ECN focusing on a multi-hole counter-bore injector, “SprayG”, in a constant-volume chamber [9]. Researchers in the ECN group provide a wide range of experimental data, such as DBIEI and Mie scattering images for the liquid phase and schlieren images for the vapor phase [10–13]. One study focused on the inner-nozzle flow and the plume-to-plume variation near the nozzle using time-resolved X-ray radiography to understand the spray rate-of-momentum effects and compare the rate-of-injection data [12]. Another study utilized DBIEI measurement for the liquid plume and further applied a three-dimensional tomographic reconstruction of ensemble-average extinction images to gain an insight into the structure and evolution of the multi-plume spray for ECN Spray G injectors with different fuels [10].

With comprehensive experimental data for validation, numerous studies have focused on numerical modeling development and spray formation under various conditions. Among all the numerical studies, there are several ways to conduct multi-phase spray simulations. These can be further categorized into two main approaches; the Eulerian-Eulerian and Eulerian-Lagrangian frameworks. The former is used to solve both liquid fuel and ambient gas phases in the Eulerian domain. The interface of the two phases is resolved by applying advection schemes such as the volume-of-fluid (VOF) method or the volume-of-fluid (VOF) method coupled with the level-set method [14]. All the associated physics from the multi-phase flow, such as primary atomization, droplet breakup, and collision, can be theoretically captured. However, a high-fidelity method of this kind requires a high resolution in space and time, and it is computationally expensive and often unaffordable for large-scale simulations. Most studies applying this type of method have focused mainly on the inner-nozzle flow [15–20]. The plume-to-plume variation and interaction in the near-nozzle regions have been extensively discussed. As the primary atomization was observed within the nozzle and in the near-nozzle region due to the counter-bore configuration of Spray G, the droplet size in either a number-based or volume-based distribution appears in several studies [15,17,19]. One study investigating the evaporation effects on different fuels, pure iso-octane and E30 (a homogeneous mixture of 30% ethanol and 70% iso-octane), revealed that the spray angle and the plume structure differs due to different viscosity and volatility [16]. The studies above provide valuable information and constructive guidance for researchers and engineers focusing on large-scale spray simulation, given that all focus on the inner-nozzle flow and the flow in the near-nozzle region (less than 6 mm from the injector).

The Eulerian-Lagrangian framework, meanwhile, is most widely employed in multi-phase spray simulations. The liquid fuel represents and is modeled as stochastic Lagrangian parcels, whereas the Eulerian domain directly solves the gaseous field. Therefore, the exchange of momentum, heat, and mass between the liquid and gas phases needs to be modeled. Since liquid fuel is tracked by the Lagrangian parcels and behaves discretely from the Eulerian domain, the temporal and spatial resolution requirement is less demanding. Numerous studies based on the Eulerian-Lagrangian framework focus on modeling the development and spray formation. They developed CFD frameworks for Spray G using Reynolds-averaged Navier Stokes (RANS) simulation and validating the framework using experimental data provided by ECN under various conditions [20–23]. Spray G has also been applied in an DISI engine [24]. One study utilizing RANS simulation investigated spray formation and spray-flow interaction using Spray G mounted inside a DISI engine under early-injection conditions [25].

Most of the research above focused on RANS simulation, while just a few applied Large Eddy Simulation (LES) [26], as most of the models for Lagrangian parcels are based on RANS simulation. LES simulation is highly dependent on the computational grid, and it can

yield uncertainties when the size disparity between the Lagrangian parcels and the Eulerian grids is trivial. Several works have used Direct Numerical Simulation (DNS) to study how the parcel and grids ratio affects droplet evaporation [27,28]. The grid dependency on droplet evaporation can be mitigated when the ratio between the Lagrangian parcels and the Eulerian grids is above 10.

Apart from droplet evaporation, which determines the heat and mass exchange between the discrete liquid parcels and the carrier gas phase, the momentum exchange is modeled by calculating the drag coefficient. Further, the drag coefficient profile depends on the sphericity of the droplet. The most popular assumption is to assume that the liquid parcels are the rigid spherical spheres and apply a correlation proposed by Amsden et al. [29]. This assumption is to be questioned in real engine environments with high ambient pressure and temperature [30,31]. To consider how the droplets' sphericity influences the drag coefficient, one study proposed a correlation considering the droplet distortion by providing a non-dimensional droplet distortion factor dynamically calculated by the Taylor Analogy Breakup (TAB) model [32] to correct the sphere drag coefficient [33].

Breakup models are imperative in spray simulations using the Eulerian-Lagrangian approach. The liquid droplets ejected from the high-pressure injector, such as gasoline spray and diesel spray, contain droplet dynamics that behave in non-equilibrium with the local gas-phase flow. Thus, the droplets undergo drop deformation, oscillation, and a variety of breakup events based on their local gas Weber number (We). These phenomena require a breakup model to reproduce as the droplets are solved and modeled in the form of Lagrangian parcels. Two models are widely accepted and applied extensively in academia and industry. One is the TAB model [32], which is built on Taylor's analogy between drop dynamics and a forced spring-mass-damper system [34]. The other is the WAVE breakup model, with its breakup mechanism derived by analogy to Kelvin-Helmholtz and Rayleigh-Taylor instability [35]. This model assumes that the breakup mechanism is determined by the wave growth rate and wavelength of Kelvin-Helmholtz and Rayleigh-Taylor instability and that the breakup time and drop size are proportional to the wave growth rate and wavelength. The WAVE breakup model (KH-RT model) has been successfully applied to the diesel spray simulation. However, it does not explicitly model the drop deformation and oscillation. The liquid droplet in a low We regime tends to undergo oscillation and deformation instead of breaking up [36,37]. This phenomenon occurs particularly in gasoline sprays with low injection pressure.

So far, the above studies convey the evolution of Eulerian-Lagrangian spray simulations from RANS simulation toward LES simulations and how models have improved from simple ones to complex ones. However, there is still a gap when it comes to combining all the knowledge acquired above and developing a suite of CFD approaches for GDI sprays using LES simulation. Furthermore, several studies have proven the competence of the models applied for GDI sprays by merely comparing the global penetration length. There are no studies that provide a comprehensive comparison, using all the possible data acquired from [9]. The objectives of this study are listed below:

1. Investigate the physics of the inner-nozzle flow and apply the essential parameters, such as the droplet distribution, plume cone angle, and plume direction, to the Eulerian-Lagrangian simulation.
2. Investigate the spray characteristics and assess the proposed framework under early- and late-injection conditions.
3. Examine different injection distribution models (blob and statistics-based droplet distribution methods) under early- and late-injection conditions.

According to the objectives above, the study will start with numerical methodologies, including governing equations of the Eulerian field and Lagrangian parcels, and the relevant equations of the models applied in the proposed framework. The validation cases and a brief

overview of the available experimental reference are performed. Thereafter, the investigation and assessment of the proposed CFD framework are described. The observation from the inner-nozzle flow is presented. The simulation based on the proposed CFD framework using different injection distribution models will then be validated and compared under early- and late-injection conditions.

## 2. Numerical methodologies

This section introduces the numerical methodologies for the proposed CFD framework based on the Eulerian-Lagrangian approach using an open-source CFD software, OpenFOAM v2012. The liquid fuel is tracked inside the stochastic Lagrangian parcels. In contrast, the ambient gas is solved in the Eulerian domain. To achieve this, Large Eddy Simulation (LES) is utilized in this study. The momentum, heat, and mass exchange of the ambient gas can be resolved by applying sufficient spatial and temporal resolution. However, those exchanges between the liquid and gas phases are not resolved and need to be modeled. They are described as source terms and solved using equations of the mass, momentum, energy, and species transport conservation in the gas phase. The governing equations, Lagrangian source terms, and the corresponding models, including drag, evaporation, heat transfer, and breakup models, will be illustrated in the subsequent subsections.

### 2.1. Gas phase-governing equations and sub-grid viscosity model

The gaseous turbulent flow in the Eulerian-Lagrangian approach is resolved using equations for the filtered compressible mass, species mass fractions, momentum, and energy in the Eulerian domain. The governing equations in Cartesian coordinates are expressed as:

$$\frac{\partial \bar{\rho}}{\partial t} + \frac{\partial \bar{\rho} \bar{u}_i}{\partial x_i} = \bar{S}_\rho, \quad (1)$$

$$\frac{\partial \bar{\rho} \bar{Y}_k}{\partial t} + \frac{\partial (\bar{\rho} \bar{u}_i \bar{Y}_k)}{\partial x_i} = \frac{\partial}{\partial x_i} [\bar{\rho} (\bar{u}_i \bar{Y}_k - \bar{u}_i \bar{Y}_k)] + \bar{\rho} \bar{D} \frac{\partial^2 \bar{Y}_k}{\partial x_i^2} + \bar{S}_{Y_k} \quad (2)$$

$$\frac{\partial \bar{\rho} \bar{u}_i}{\partial t} + \frac{\partial (\bar{\rho} \bar{u}_i \bar{u}_j)}{\partial x_i} = \frac{\partial}{\partial x_i} [\bar{\rho} (\bar{u}_i \bar{u}_j - \bar{u}_i \bar{u}_j)] + \bar{\tau}_{ij} - \frac{\partial \bar{p}}{\partial x_i} + \bar{S}_{u_i} \quad (3)$$

$$\frac{\partial \bar{\rho} \bar{h}_t}{\partial t} + \frac{\partial (\bar{\rho} \bar{u}_i \bar{h}_t)}{\partial x_i} = \frac{\partial \bar{p}}{\partial t} + \frac{\partial}{\partial x_i} [\bar{\rho} (\bar{h}_s \bar{h}_s - \bar{h}_s \bar{h}_s)] + \bar{\mu} \frac{\partial \bar{h}_s}{\partial x_i} + \bar{S}_{h_t} \quad (4)$$

where  $(\bar{\cdot})$  and  $(\tilde{\cdot})$  denote the filter and Favre filter operator.  $\rho$ ,  $u$ ,  $p$ ,  $Y_k$ ,  $h_t$  and  $h_s$  denote the density, velocity, pressure, mass fraction, total enthalpy and sensible enthalpy, respectively.

Eqs. (2), (3) and (4) need to be closed by introducing an eddy viscosity model:

$$\bar{\rho} (\bar{u}_i \bar{u}_j - \bar{u}_i \bar{u}_j) = -2\mu_t (\bar{S}_{ij} - \frac{1}{3} \bar{S}_{kk} \delta_{ij}) \quad (5)$$

$$\bar{\rho} (\bar{h}_s \bar{h}_s - \bar{h}_s \bar{h}_s) = \frac{\mu_t}{Pr_t} \frac{\partial \bar{T}}{\partial x_i} \quad (6)$$

$$\bar{\rho} (\bar{Y}_k \bar{Y}_k - \bar{Y}_k \bar{Y}_k) = \frac{\mu_t}{Sc_t} \frac{\partial \bar{Y}_k}{\partial x_i} \quad (7)$$

$\bar{S}_{ij}$  is the resolved strain rate tensor  $\bar{S}_{ij} = 0.5(\partial \bar{u}_i / \partial x_j + \partial \bar{u}_j / \partial x_i)$ .  $Pr_t$  and  $Sc_t$  refer to modeled Prandtl and Schmidt numbers, respectively. The sub-grid eddy viscosity  $\mu_t$  is acquired from the static sigma model [38].

In Eqs. (1) to (4), the filtered source terms,  $\bar{S}_\rho$ ,  $\bar{S}_{Y_k}$ ,  $\bar{S}_{u_i}$ , and  $\bar{S}_{h_t}$ , are acquired from the Lagrangian framework through different models, such as evaporation, drag and heat transfer. All the corresponding models will be discussed in the following section.

### 2.2. Liquid phase-governing equations

The governing equations for the instantaneous Lagrangian motion within the OpenFOAM framework appearing as source terms from Eqs. (1) to (4) exhibit:

$$\bar{S}_\rho = -\frac{1}{\Delta V} \sum_{i=1}^N \frac{dm_p}{dt} \quad (8)$$

$$\bar{S}_{Y_k} = -\frac{1}{\Delta V} \sum_{i=1}^N \frac{dm_{p_k}}{dt} \quad (9)$$

$$\bar{S}_u = -\frac{1}{\Delta V} \sum_{i=1}^N \frac{d(m_p u_p)}{dt} \quad (10)$$

$$\bar{S}_{h_t} = -\frac{1}{\Delta V} \sum_{i=1}^N \frac{d(c_p m_p T_p)}{dt} \quad (11)$$

where  $\Delta V$  and  $N$  represent the volume of the Eulerian cell where the Lagrangian parcels dwell and the total number of the Lagrangian parcels within the Eulerian cell, respectively.

The velocity of liquid droplets tracked statistically in each Lagrangian parcel is solved as follows:

$$\frac{du_p}{dt} = \frac{3}{4} C_D Re_p \frac{\mu_g}{\rho_p d_p^2} u_{rel} + g, \quad (12)$$

where  $(.)_p$  denotes the properties of the liquid parcels, while  $(.)_g$  represents gas properties.  $u_{rel}$  is the relative velocity from the ambient gas and a parcel,  $u_{rel} = u_g - u_p$ .  $g$  is the gravitational acceleration. The drag coefficient ( $C_D$ ) needs to be acquired by drag models.

The rate of mass transfer to the drop surface is written as follows:

$$\frac{dm_p}{dt} = \pi d D_p S h_p \ln(1.0 + BM), \quad (13)$$

where  $S h_p$  is the Sherwood number from the liquid parcel, and the Spalding mass transfer number ( $BM$ ) is defined as

$$BM = \frac{Y_s - Y_G}{1.0 - Y_s}, \quad (14)$$

where  $Y_s$  refers to the fuel vapor mass fraction on the parcel surface, and  $Y_G$  is the vapor mass fraction away from the parcel surface.

The rate of heat transfer to the drop surface is written as follows:

$$mc_p \frac{dT_p}{dt} = h A_p (T_g - T_p) - \frac{dm}{dt} h_v, \quad (15)$$

where  $A_p$  is the surface area of each Lagrangian parcel,  $h = \frac{Nu_p k_g}{d}$  is the heat transfer coefficient, and  $h_v$  denotes the heat of vaporization.

To close the Lagrangian governing Eqs. (12), (13), and (15), the drag coefficient ( $C_D$ ), Sherwood number( $S h_p$ ), and Nusselt number( $N u_p$ ) need to be specified by either models or correlations. The current approach in OpenFOAM and other CFD software assumes the liquid droplets ejected from the injectors are dispersed and behave as rigid spheres. According to the assumptions, the drag model for a rigid sphere reads [29]:

$$C_{D,sphere} = \begin{cases} \frac{24}{Re_p} (1.0 + \frac{1}{6} Re_p^{\frac{2}{3}}), & Re \leq 1000 \\ 0.424, & Re > 1000 \end{cases}, \quad (16)$$

Furthermore, according to the Frossling correlation [32] for mass and heat transfer, the Sherwood and Nusselt number can appear in the form:

$$Sh_{p,sphere} = (2 + 0.6 Re_p^{\frac{1}{2}} Sc_p^{\frac{1}{3}}), \quad (17)$$

$$Nu_{p,sphere} = (2 + 0.6 Re_p^{\frac{1}{2}} Pr_p^{\frac{1}{3}}), \quad (18)$$

where  $Sc_p$  is the liquid Schmidt number and  $Pr_p$  is the liquid Prandtl number.

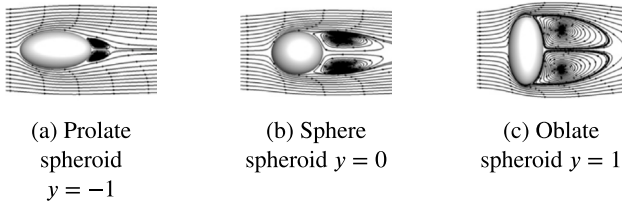


**Fig. 1.** The deformation of liquid droplets and the corresponding distortion factor ( $y$ ).  
Source: Re-printed from a study by Richter and Nikrityuk [41].

### 2.3. Distorted droplet models for momentum, heat, and mass exchange

Several studies have developed models based on empirical research or **DNS** simulation data to improve the standard drag model accounting for the effect of droplet non-sphericity [31,33,36,39]. The most popular model is the distorted sphere drag model from [33].

It provides a non-dimensional droplet distortion factor ( $y$ ) calculated dynamically using the TAB breakup model from [40] to correct the sphere drag coefficient, shown in Eq. (16).

The correction formula reads:

$$C_D = C_{D,\text{sphere}}(1 + 2.632y), \quad 0 \leq y \leq 1 \quad (19)$$

However, this model only considers the distortion for oblate spheroids. The deformation in the form of prolate spheroids, which often occurs during droplet oscillation and deformation, is neglected. Motivated by this limitation of the currently available approach, the following is to present the models considering droplet distortion effects on drag, evaporation, and heat transfer.

The distortion model utilized in this study is according to research by Richter and Nikrityuk [41]. It takes into account the deformation of prolate spheroids modeled using the TAB breakup model, as shown in Fig. 1. The study employed a **DNS** simulation to derive a regression model that is capable of predicting 99.8% of the variance in the drag coefficient and appears as:

$$\frac{C_D}{C_{D,\text{sphere}}} = \frac{0.21 + \frac{20}{Re_p}(\frac{l}{d})^{0.58} + \frac{6.9}{\sqrt{Re_p}}(\frac{l}{d})^{-1.4}}{0.21 + \frac{20}{Re_p} + \frac{6.9}{\sqrt{Re_p}}}, \quad (20)$$

where  $l$  denotes the spanwise length of the droplets and appears in the form:

$$l = d(1 - C_b y), \quad (21)$$

where  $C_b$  is a model constant with a value equal to 0.5.

As the oscillation and deformation of the liquid droplets occur, the surface area is no longer equal to the sphere surface. This phenomenon affects the Nusselt number ( $Nu_p$ ). Richter and Nikrityuk also provided a correlation by identifying the sphericity ( $\phi$ ) and the crosswise sphericity ( $\phi_\perp$ ), shown as:

$$\frac{Nu_p}{Nu_{p,\text{sphere}}} = \frac{1.76 + 0.55\phi Pr_p^{\frac{1}{3}} Re_p^{\frac{1}{2}} \phi_\perp^{0.075} + 0.014 Pr_p^{\frac{1}{3}} Re_p^{\frac{2}{3}} (\frac{\phi}{\phi_\perp})^{7.2}}{1.76 + 0.55 Pr_p^{\frac{1}{3}} Re_p^{\frac{1}{2}} + 0.014 Pr_p^{\frac{1}{3}} Re_p^{\frac{2}{3}}}, \quad (22)$$

where the sphericity ( $\phi$ ) and the crosswise sphericity ( $\phi_\perp$ ) are defined as:

$$\phi = \frac{4\pi r_p^2}{SrfC_p}, \quad (23)$$

$$\phi_\perp = \left(\frac{r_p}{H}\right)^2, \quad (24)$$

In Eqs. (23) and (24),  $H$  and  $SrfC_p$  are half length of the crosswise axis relative to the flow direction of the droplet and the surface area of the droplet, respectively. These two parameters exhibit:

$$H = \sqrt{\frac{r_d^3}{r(1 - C_b y)}}, \quad (25)$$

where  $r$  is the radius of the droplet.

$$SrfC_p = \begin{cases} 2\pi H^2(1 + \frac{1-e^2}{e} \tanh^{-1}(e)), & y \geq 0 \\ 2\pi H^2(1 + \frac{r(1-C_b)y}{He} \sinh^{-1}(e)), & y < 0 \end{cases}, \quad (26)$$

with the eccentricity  $e$  defined as

$$e = \sqrt{1 - (\frac{\min(H, 0.5l)}{\max(H, 0.5l)})^2}, \quad (27)$$

It is not the first time that the correlations above have been applied to spray research. They have been utilized in the **ECN** group for a swirl-type spray under engine-like conditions [36], and **ECN** diesel spray (Spray A) [31]. However, the **ECN** group combined the correlations with a model considering the viscous effects of droplets from [42,43]. Details on the combined model, the so-called “Corrected Distortion model”, based on Converge CFD Software, can be found in several studies [26,31,36].

Furthermore, the improved evaporation model is deployed by utilizing the non-equilibrium evaporation model considering the Langmuir-Knudsen law [44,45]. This model does not consider the superheated conditions in which the droplet encounters flash boiling. The evaporation only takes place on the surface of the droplet, assuming that the droplets are spherically symmetric and that the temperature at the droplet surface is continuous. Unlike the standard model, the non-equilibrium evaporation model does not assume that the droplet surface is in thermodynamic equilibrium, in which case the mole fraction of fuel vapor can be obtained in relation to the saturated pressure using the Clausius-Clapeyron equation. The vapor mole fraction in this non-equilibrium evaporation model reads:

$$X_{s,\text{neq}} = X_{s,\text{eq}} - \left(\frac{L_K}{D/2}\right)\beta, \quad (28)$$

where  $X_{s,\text{eq}}$  is the equilibrium vapor mole fraction and can be obtained by the Clausius-Clapeyron equation.  $L_K$  is the Knudsen layer thickness.

$$L_K = \frac{\mu \sqrt{2\pi T_p \bar{R}/W_v}}{Sc_p p}, \quad (29)$$

where  $\bar{R}$ ,  $T_p$ , and  $p$  are the gas constant, droplet temperature, and gas pressure, respectively. The non-dimensional evaporation parameter,  $\beta$ , is given by

$$\beta = -\left(\frac{3Pr\tau_p}{2}\right) \frac{\dot{m}_p}{m_p}, \quad (30)$$

where  $\tau_p$  is the parcel time constant for the Stokes flow and can be defined as

$$\tau_p = \rho_p d^2 / (18\mu), \quad (31)$$

Eq. (28) can be further manipulated to mass fraction to calculate the Spalding mass transfer number (BM) in Eq. (14). A solution to Lagrangian grid dependency is also applied in this evaporation model. Hinrichs et al. [28] investigated the droplet evaporation under both non-convective and convective conditions. The study shows that if the ratio of the Lagrangian droplet diameter to the grid size is less than 10, it will yield over-evaporated results. This observation agrees well with another study on a swirling combustor using **DNS** simulation by Luo et al. [27]. To mitigate this phenomenon, Hinrichs et al. [28] proposed a correction in Eq. (13), and the modified mass rate exchange equation reads:

$$\frac{dm_p}{dt} = \pi d D_p S_h \ln(1.0 + BM) \frac{(\Delta + r)}{\Delta}, \quad (32)$$

where  $\Delta$  is the grid size.

The factor goes to unity when the droplet size is much smaller than the grid size ( $r \ll \Delta$ ). By contrast, it becomes larger than unity to compensate for the liquid vaporization when the droplet size is much bigger than the grid size ( $r \gg \Delta$ ).

## 2.4. Breakup model

This study employs the WAVE breakup model proposed by Patterson and Reitz [35]. Within this model, the breakup mechanism is triggered by the competition between the growth rate and wavelength of Kelvin-Helmholz and Rayleigh-Taylor instability. The essential parameters,  $B_0$ ,  $B_1$ , and  $C_{rt}$ , are ad hoc and often appear in different values with different studies about the same application. Thus, the corrections proposed by Nagaoka and Kawamura [46] can be applied to avoid extensive parameter tuning effort, especially for low Weber number conditions. The corrections are calculated based on the local gas Weber number ( $We$ ) and appear in the form:

$$B_0 = 0.61(1 - 1.43(\frac{\rho}{\rho_p})^{0.2} \exp(-\frac{We}{10})), \quad (33)$$

$$B_1 = 161.7 \sqrt{\frac{\rho}{\rho_p}} \min(1, (\frac{15}{We})^{0.8}), \quad (34)$$

$$C_{rt} = \max(0.2, (0.11\sqrt{We})), \quad (35)$$

Furthermore, Nagaoka and Kawamura [46] combined the WAVE breakup model and the correlations proposed by Pilch and Erdman [47] to consider the droplet deformation. The combined WAVE breakup model with dynamic corrections has been validated in research of GDI swirl-type injectors and is successfully applied to a ECN Spray G study [25].

## 2.5. Injection distribution model

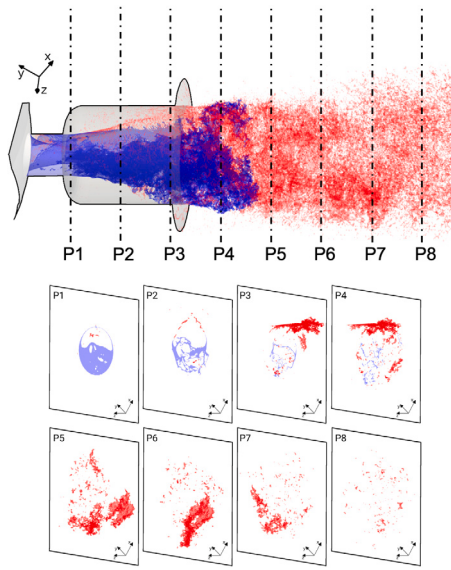
The distribution model of the Eulerian-Lagrangian approach determines the initial size of the Lagrangian parcels ejected from the injector. Often, researchers and engineers are not aware of the geometry of the inner nozzle and the flow mechanism of the inner-nozzle flow. Moreover, conducting a reliable inner-nozzle flow simulation and near-nozzle measurement is expensive and time-consuming. It is challenging to provide a droplet size distribution. The most popular method, proposed by Reitz and Diwakar [48], assumes that the ejected drops ("blobs") from the injector are equal in size to the nozzle diameter. This is called the blob method. This model has been proven to predict the penetration length correctly in high-pressure sprays [21,23,25,26,31, 49]. However, it can yield uncertainties when the targeted spray has a counter-bore inner nozzle, such as ECN Spray G. Often, the unphysical sharp tip at the spray downstream can be observed even though the global penetration length is captured [23,25]. Several studies devoted attention to the inner-nozzle flow of the ECN Spray G and discovered that the size of the droplets is much smaller than the nozzle diameter, as most primary atomization takes place within the inner nozzle and near-nozzle region [17,19,20,50].

Fig. 2 shows the evolution of the droplet dynamics along the injector axis acquired from a DNS simulation [50]. The location of P8 is 1 mm from the nozzle exit. The liquid droplets in the blue region are still within the liquid core, whereas the red region indicates that the liquid ligament breaks up and the droplets detach from the liquid core. Evidently, the liquid core only exists up to 0.4 mm from the nozzle exit. The liquid ligament breakup almost completes after P5. Therefore, this study develops a CDF for the droplet size distribution derived from the DNS data to mitigate the uncertainty yielded by the blob method.

Fig. 3 shows the droplet size distribution function in section plane P6. It reveals that the droplet size is less than 25  $\mu\text{m}$ , and the majority of the droplet size (40% of the distribution) is approximately between 5  $\mu\text{m}$  to 10  $\mu\text{m}$ . This reaches an agreement with experimental data from ECN [10,13]. The droplet size distribution function reads:

$$d(x) = 1.569 \exp(1.823x) + 5.185 \exp(30.88x), \quad (36)$$

where  $x \in [0, 1]$  is an uniform random number.



**Fig. 2.** Evolution of the droplet dynamics along the injector axis with eight different sections [50]. (note: with an uniform distance of 0.2 mm between each section; blue color indicates the spray liquid core, whereas the red one represents the liquid droplets.). (For interpretation of the references to color in this figure legend, the reader is referred to the web version of this article.)

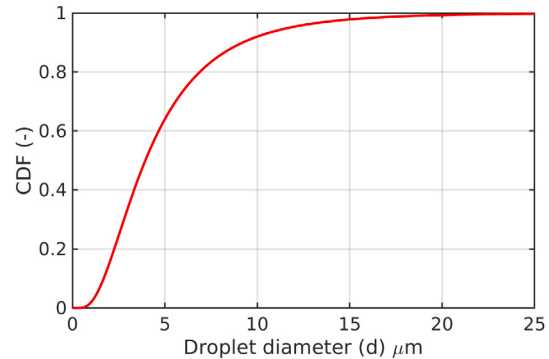


**Fig. 3.** Cumulative distribution function (CDF) of the droplet size distribution at section P6, shown in Fig. 2.

## 3. Validation cases and numerical setup

This study focuses on the GDI spray provided by ECN. The GDI spray, referred to as "Spray G", operates within a hole-type injector featuring an eight-hole counter-bore configuration with injection pressure up to 200 bar. According to available experimental data from [9], the operating conditions of Spray G covered not only early- and late-injection conditions but also the critical conditions within the flash boiling regime. Furthermore, two different fuels are studied, pure iso-octane and a surrogate gasoline fuel (E00). This study focuses on pure iso-octane. All the available operating conditions distribute over the diagram of ambient pressure against fuel temperature, shown in Fig. 4.

Fig. 4 depicts all the available data from ECN, and further, the data is categorized with numbers from one to three. The regime below the boiling curve represented as the black line in Fig. 4 is the flash boiling regime. In this regime, droplets experience substantial evaporation, encompassing both heat exchange at the droplet surface and internal heat exchange due to bubble nucleation, growth, and breakup within the droplet. Although there are numerous models accounting for flash boiling for spray simulations, all pertain to specific applications with limitations and incomplete assumptions [52,53]. Thus, the proposed

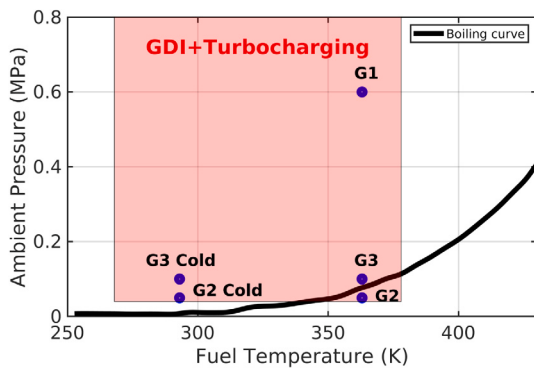


**Fig. 4.** Available operating conditions of Spray G within p-T diagram of iso-octane; the red patch denotes the possible conditions for the GDI engine with turbocharging. (For interpretation of the references to color in this figure legend, the reader is referred to the web version of this article.)  
Source: Re-plotted from [51].

**Table 1**  
Essential parameters of the three operating conditions.

Spray G (Iso-octane)	G1	G3	G3 Cold
Injection condition	Late	Early	Early
Fuel temperature (K)	363	363	293
Injection pressure (bar)	200	200	200
Ambient temperature (K)	573	333	293
Ambient pressure (bar)	6	1	1

CDF framework devotes attention to the non-flash boiling conditions, and both high- and low-load conditions are considered, termed G1, G3, and G3 Cold. All the essentials of the three targeted conditions are shown in Table 1.

### 3.1. Experimental measurement and data

The experimental data from ECN are acquired by means of Diffused backlight illumination extinction imaging (DBIEI) measurement for the liquid phase and schlieren measurement for the vapor phase. The laser signal intensity from DBIEI measurement varies based on the extinction threshold. Furthermore, schlieren's (beam-steering) effects can be mitigated by applying the light diffuser to obtain a proper diffusion angle [13,54,55]. Rather than Mie-scattering imaging, ECN recommends DBIEI measurement as it can provide a less biased liquid boundary and is more suitable as a reference for CFD simulation as it takes into account schlieren (beam-steering) effects.

Following the assumption that scattering objects are spherical, Mie scatter extinction theory can be applied to obtain the droplets' LVF. To provide a quantitative and qualitative comparison with CFD simulation data, ECN further post-processed the liquid volume fraction (LVF) to acquire PLV images. Therefore, the liquid penetration length and possible liquid boundary can be procured through two different extinction values defined by ECN, as shown in Eq. (37). In this study, the lower threshold  $0.2 \cdot 10^{-3} \text{ mm}^3(\text{liquid})/\text{mm}^2$  was applied to process binary PLV data.

$$\text{PLV} = \int_{-y_\infty}^{y_\infty} \text{LVF} \cdot dy = 0.2 \cdot 10^{-3} \frac{\text{mm}^3(\text{liquid})}{\text{mm}^2} = 2.0 \cdot 10^{-3} \frac{\text{mm}^3(\text{liquid})}{\text{mm}^2}, \quad (37)$$

To follow the concept, "Follow the fuel", ECN utilized the ensemble-averaged PLV data from 300 injections at three different observing angles,  $0^\circ$ ,  $22.5^\circ$ , and  $45^\circ$ , to reconstruct the 3-D plume shape using 3-D computer tomographic (3-D CT) reconstruction. The image obtained at the section 30 mm below the injector is shown in Fig. 5.

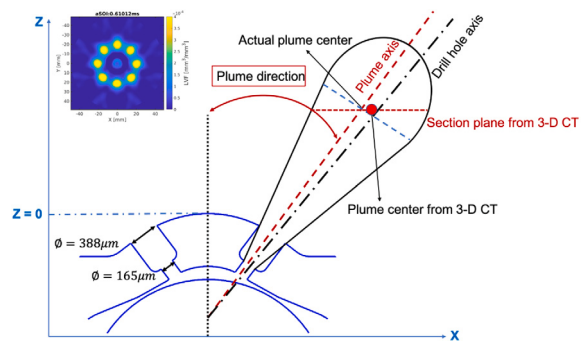


**Fig. 5.** The geometry of the Spray G and an example of 3-D computer tomographic (3-D CT) reconstruction section at  $Z = 30 \text{ mm}$  at  $\text{aSOI} = 0.61 \text{ ms}$ .

However, this technique assumes that the Spray G with an 8-hole configuration is  $45^\circ$  symmetric and requires linear interpolation to fill the gap. It also yields some uncertainties and deviations [13]. The main uncertainty is the droplet diameter  $d$  used to acquire the LVF value. As the droplet diameter  $d$  varies from region to region, the experimental data is processed using a constant droplet diameter  $d = 7 \mu\text{m}$  measured using PDI [10]. Follow this procedure, the produced LVF signal is often underpredicted. Furthermore, the deviation is that the maximum signal pivot point is not always a plume center as the plume axis is not perpendicular to the plume section, as shown in Fig. 5. Despite all the uncertainties and deviations, the processed 3-D computer tomographic reconstruction data is still reliable regarding the location of the maximum signal pivot point and plume directions [10,13].

In this study, all the simulation data are post-processed in the same manner using Python scripts provided by ECN to deliver a consistent dataset for comparison. The procedure is shown in Fig. 6. The extinction threshold for the numerical liquid boundary from PLV and the vapor boundary projected using schlieren probabilities are set to  $0.2 \cdot 10^{-3} \text{ mm}^3(\text{liquid})/\text{mm}^2$  and  $1.0 \cdot 10^{-3} \text{ mm}^3(\text{vapor})/\text{mm}^2$ , respectively.

### 3.2. Numerical setup

This study performs simulations in a computational domain close to the ECN constant-volume chamber, allowing observation of the whole evolution of spray under different operating conditions. The computational domain in this study is set up as a cube with a dimension 100 mm. The meshing strategy is to apply a static mesh with the coarsest mesh size  $1000 \mu\text{m}$  to the finest mesh size  $125 \mu\text{m}$  to resolve the turbulence induced by spray. Therefore, the total number of computational grids is 15 million. The computational domain and mesh details are shown in Fig. 7.

The simulation is grid-dependent as the study utilizes Large Eddy Simulation (LES). The mesh quality assessment is carried out using the viscosity ratio proposed by Celik et al. [56] as a criterion for the resolution of LES. The detail is described, and the results are shown in Appendix A. The Eulerian-Lagrangian approach requires not only the mesh quality of the gas phase but also the essential parameters of the targeted injector as inputs for the Lagrangian fields. The essential parameters of the ECN Spray G, such as mass flow rate, plume cone angle, and direction, in this study, are summarized in Table 3 and Fig. 8.

The simulation is conducted using a developed-code library based on an open-source CFD software, OpenFOAM v2012. The discretization schemes for temporal and spatial are up to second-order accuracy. The total simulation time is two times of injection duration, which is 1.56 ms. In this study, several cases will be involved in the investigation by comparing them with experimental results under early- and late-injection conditions. To clarify each case, Table 2 categorizes all the participating cases with their Lagrangian models and simulating conditions. All these cases will be mentioned with its label in the subsequent section.

**Table 2**

Models and simulating conditions for each participating case.

Cases(-)	Conditions	Injection model	Breakup model	Evaporation model	Drag model	Heat transfer
Case 1	G3	Eq. (36)	Eqs. (33) to (35)	Eq. (32)	Eq. (20)	Eq. (22)
Case 2	G3	blob method ( $d = 165 \mu\text{m}$ )	Eqs. (33) to (35)	Eq. (32)	Eq. (20)	Eq. (22)
Case 3	G3 Cold	Eq. (36)	Eqs. (33) to (35)	Eq. (32)	Eq. (20)	Eq. (22)
Case 4	G1	Eq. (36)	Eqs. (33) to (35)	Eq. (32)	Eq. (20)	Eq. (22)
Case 5	G1	blob method ( $d = 165 \mu\text{m}$ )	Eqs. (33) to (35)	Eq. (32)	Eq. (20)	Eq. (22)
Case 6 [49]	G1	blob method ( $d = 165 \mu\text{m}$ )	KH-RT	CD-Frossling	CD model	Eq. (22)

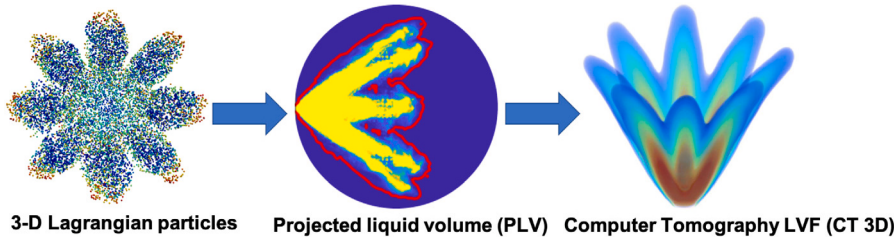


Fig. 6. The procedure to post-process the simulation data, PLV and 3-D LVF, for comparison.

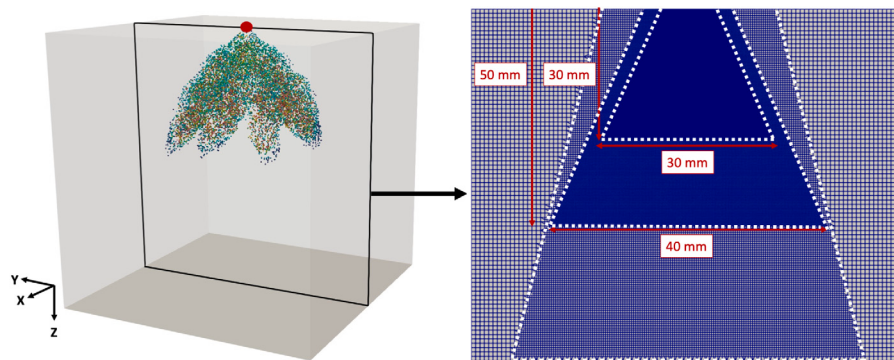


Fig. 7. The computational domain and mesh details for ECN Spray G (The center of the injector is set up at the origin of the computational domain, which is marked as a red circle) (note: the white broken line is to outline the mesh refinement). (For interpretation of the references to color in this figure legend, the reader is referred to the web version of this article.)

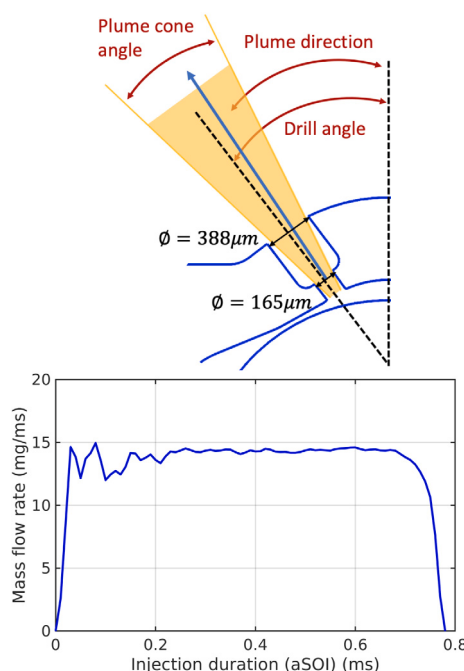


Fig. 8. The ECN Spray G injector schematic defines the essential parameters in Table 3, and the mass flow rate.

**Table 3**

Essential parameters of ECN Spray G injector.

Parameters of the injector for simulation input

Total injected mass (mg)	10
Plume cone angle (°)	30
Plume direction (°)	35
Injector diameter ( $\mu\text{m}$ )	388
Discharge coefficient ( $C_d$ )	0.73

## 4. Results

This section will transition from examining the inner-nozzle flow characteristics to encompassing the entire spray evolution. Thereafter, a validation of the proposed approach under early-injection conditions (Spray G3 and Spray G3 Cold) is to be carried out. An assessment of different injection distribution models is then conducted. The investigation will further move toward the spray under late-injection conditions (Spray G1). Due to stronger evaporation, the liquid phase extinction and Sauter mean diameter (SMD) are the subjects to be discussed.

### 4.1. Early-injection conditions (Spray G3 and Spray G3 Cold)

#### 4.1.1. Spray characteristics and validation

This section focuses on Spray G under early-injection conditions, as shown in Table 1. Under these conditions, the spray is less susceptible to evaporation than Spray G1 under high-pressure, high-temperature

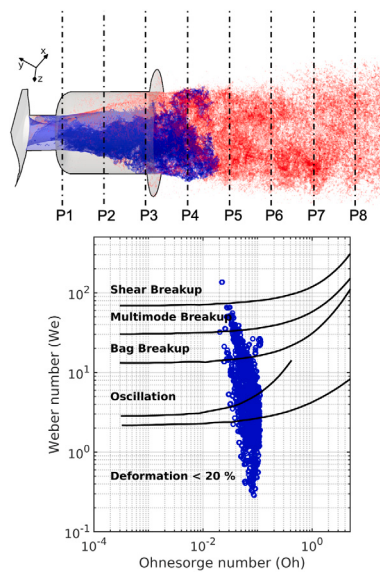


**Fig. 9.** Droplets at section P5 distributes within a breakup regime diagram based on Ohnesorge number ( $\text{Oh}$ ) and Weber number ( $\text{We}$ ) [37,50]. (For interpretation of the references to color in this figure legend, the reader is referred to the web version of this article.)

ambient conditions. Therefore, the spray ligament breakup is the main characteristic. **Fig. 9** demonstrates the liquid droplets in section P5 scattering within a breakup regime, according to the droplets' local  $\text{Oh}$  and Weber number ( $\text{We}$ ). The inner-nozzle flow simulation is conducted using DNS [50].

**Fig. 9** reveals that the majority of the droplets in section P5 (0.4 mm from the nozzle exit) lie within the bag breakup and oscillation regimes. A few droplets with their Weber number ( $\text{We}$ ) exceeding 100 may encounter a shear breakup. A three-dimensional morphology is utilized to distinguish the liquid core structure and the liquid droplets marked as blue and red, respectively. After section P6 (0.6 mm from the nozzle exit), the liquid ligament breakup completes. The proposed CFD framework applies the necessary information, such as plume direction and flow coefficient, from the DNS simulation to stimulate the spray evolution of the standard Spray G under early-injection conditions (Spray G3). The present case is Case 1, as shown in Table 2. **Fig. 10** depicts the spray at  $\text{aSOI} = 0.58 \text{ ms}$  and the breakup regimes of droplets at certain regions from upstream to downstream.

In **Fig. 10**, the liquid droplets follow the previous pathway from the inner-nozzle flow simulation and start to break up into small droplets. The droplet dynamics move toward the oscillation and deformation region as the Weber number ( $\text{We}$ ) decays from spray upstream to downstream. However, the corresponding Ohnesorge number ( $\text{Oh}$ ) does not have significant change, and yet the droplets lie within a range  $0.03 < \text{Oh} < 0.05$ . According to the breakup regime, shown in **Fig. 10(b)** and (c), the Ohnesorge number has trivial impacts on the identified drop dynamics only if the Ohnesorge number ( $\text{Oh}$ ) below unity. It can be explained that the droplets, after injection, experience droplet breakup and oscillation and further lose their momentum. However, the ratio of the viscous force to the inertial force and surface tension remains balanced. **Fig. 10** indicates that droplet deformation plays a crucial role in Spray G.

**Fig. 11** provides a quantitative comparison with experimental data. The liquid and vapor phases are compared. The difference between Spray G3 and Spray G3 Cold is the injection and ambient temperatures, highlighted in Table 1. In the Spray G3 case, the ambient temperature is 40 K higher than the Spray G3 Cold case, and it is close to the boiling temperature of iso-octane ( $T_{\text{boil}} = 372 \text{ K}$ ). Under these conditions, the evaporation effect becomes significant in the spray evolution, as

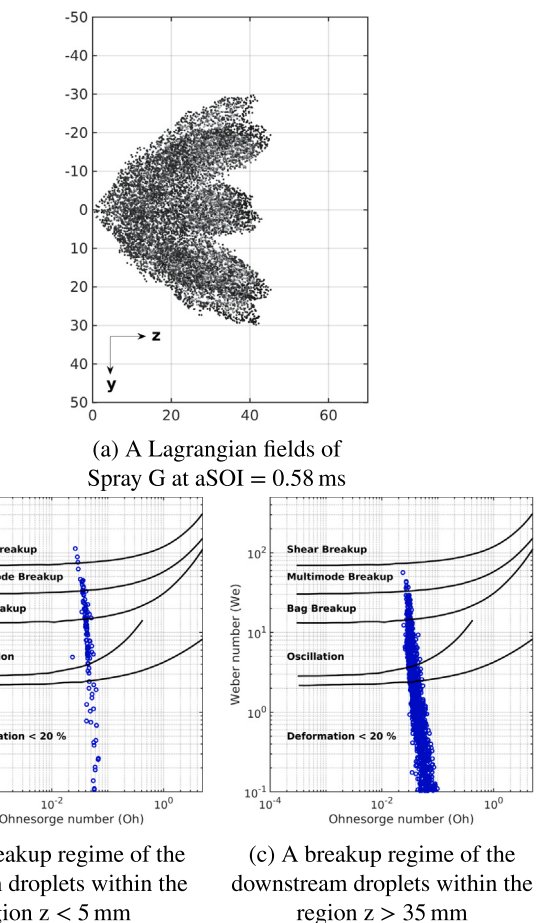


**Fig. 10.** Demonstration of the spray droplets distribution of Case 1 within the breakup regime diagram of Hsiang and Faeth [37].

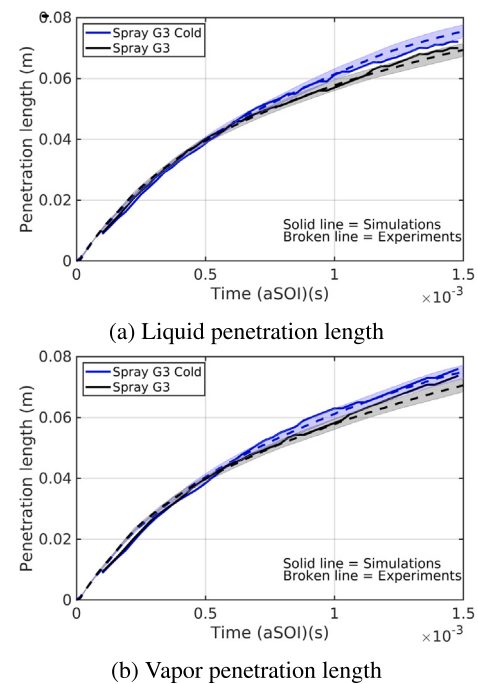


**Fig. 11.** Quantitative comparison of the liquid and vapor penetration length. Both conditions (Spray G3 and Spray G3 Cold) are involved. The two cases are referred to as Case 1 and Case 3, shown in Table 2.

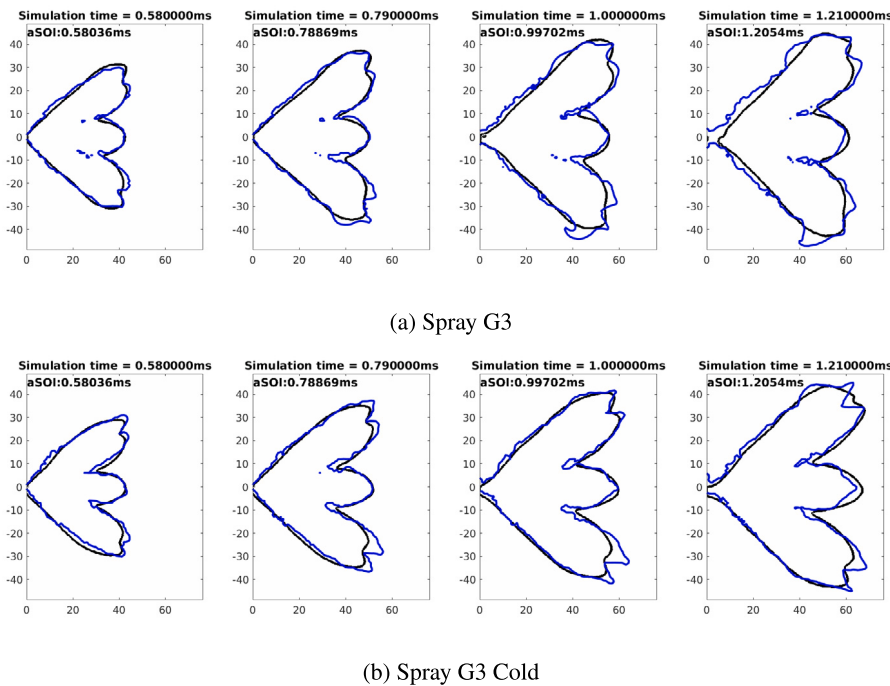


**Fig. 12.** Qualitative comparison of the projected liquid boundary measured by DBIEI with extinction threshold equal to  $0.2 \cdot 10^{-3}$  ( $\text{mm}^3(\text{liquid})/\text{mm}^2$ ). Black line: the experimental data, Blue line: the simulation data. (For interpretation of the references to color in this figure legend, the reader is referred to the web version of this article.)

evident in Fig. 11. Despite the influence of evaporation, it is unlikely for the fuel iso-octane to completely vaporize. Consequently, the penetration of both liquid and vapor remains comparable. Notably, the simulation data demonstrate a strong agreement with the experimental data in both cases. However, it is challenging to precisely quantify the impact of evaporation and establish the accuracy of the simulation merely based on the penetration length. For a qualitative assessment, Fig. 12 presents a comparison of the liquid plume boundary using the projected liquid volume data (PLV).

The evaporation effect can be observed in the liquid plume boundary, as shown in Fig. 12. Due to the minor evaporation effect, the liquid plume boundary in Spray G3 cold case is more intact, and no plume detachment appears at  $\text{aSOI} = 1.21$  ms compared with the Spray G3 case. The evaporation effect can be captured by the simulation. The numerical spray plume tips downstream in Spray G3 Cold case are more revealing than Spray G3. The under-prediction of liquid penetration length at  $\text{aSOI} = 1.21$  ms in the Spray G3 Cold case also appears in Fig. 11. To provide a complete analysis and a comprehensive comparison, Fig. 13 provides a qualitative comparison of vapor schlieren probability images.

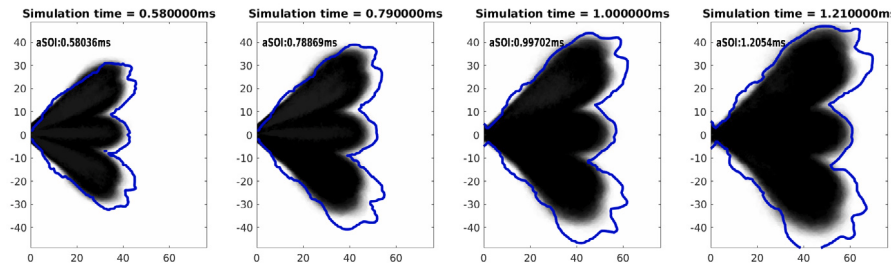
In Fig. 13, the vapor plume is more dispersed in the Spray G3 case, and the spray tips are more round than in the Spray G3 Cold case. A phenomenon of this kind also appears even more significantly in numerical spray plumes. Interestingly, in the Spray G3 case, the simulation results, albeit more dispersed and wide spray plumes, do not overpredict the penetration length. However, it shows otherwise in Fig. 11, particularly after  $\text{aSOI} = 1.0$  ms. Fig. 14 provides a more direct comparison of the evaporation effect between these two cases by demonstrating the liquid mass ratio, which is the current liquid fuel mass in the constant-volume chamber normalized by the overall injected mass (10 mg). Both profiles reach the peak at  $\text{aSOI} = 0.78$  ms, which is the overall injection duration. Despite following the same trend, Spray G3 contains only 45% of the liquid mass at the end of the injection duration, while Spray G3 Cold has almost 85% of the liquid mass within the constant-volume chamber. The contained liquid mass in Spray G3 vaporizes exponentially in the aftermath of the injection.

#### 4.1.2. Assessment of injection distribution models

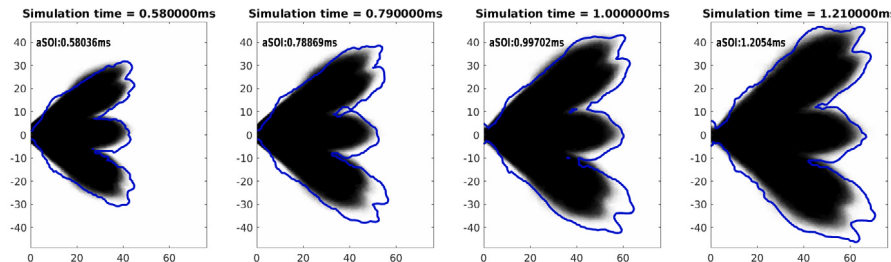
Efforts, by far, have been dedicated to comparing experimental data and the proposed CFD framework, and, further, focusing on the spray characteristics under different conditions. It is evident that due to the counter-bore inner-nozzle configuration, the primary atomization takes place in the inner-nozzle region. This mechanism, consequently, triggers the liquid core breakup in the vicinity of the nozzle exit, as shown in Fig. 9. The conventional injection distribution model, commonly referred to as “the blob method”, assumes that the ejected droplets are uniformly distributed and behave as a “blob” with a size equivalent to the nozzle diameter. This widely accepted model has found success in both academic and industrial applications. However, under this assumption, the droplet size is approximately 10 to 20 times larger than the observed droplet sizes obtained from experiments and simulations. This section will carry out a comprehensive comparison between the blob method and the proposed statistical droplet distribution method. The two cases are referred to as Cases 1 (CDF) and 2 (blob method), as shown in Table 2. Both utilize the same framework for the rest of the Lagrangian models proposed in Section 2 to deliver a fair comparison. The presented assessment is based on the Spray G3 case. Fig. 15 compares the different droplet distribution models in the liquid phase.

By using the blob method, the penetration length is in good agreement with experimental data, even though some minor overprediction appears after  $\text{aSOI} = 0.76$  ms. To quantify the deviation between the numerical and experimental results, Fig. 15(b) presents a comparison using the Root-mean-square deviation (Root-mean-square deviation (RMSD)) for the global penetration length. Both simulation datasets closely match the experimental data, with RMSD values below 1%. However, the blob method yields more than two times higher RMSD compared to Case 1.

Moreover, the generated spray plume shape from Case 2 is relatively wide, and the spray plume tips downstream are unphysically sharp. In the previous discussion in Section 4.1.1, The sharp tip can be observed in the Spray G3 Cold case experimentally and numerically owing to the evaporation effect, shown in Fig. 12. It is, however, absent in the Spray G3 case. The cause of the disparity between the plume shapes



(a) Spray G3



(b) Spray G3 Cold

**Fig. 13.** Qualitative comparison of the projected vapor schlieren probability images with extinction threshold equal to  $1.0 \cdot 10^{-3}$  ( $\text{mm}^3(\text{vapor})/\text{mm}^2$ ). Black image: the experimental data, Blue line: the simulation data. (For interpretation of the references to color in this figure legend, the reader is referred to the web version of this article.)

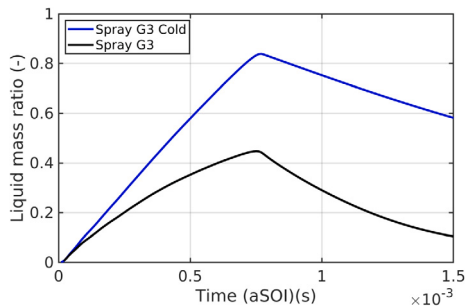


**Fig. 14.** Time evolution of the liquid mass ratio( $\text{mass}_{\text{liquid}}/\text{mass}_{\text{total}}$ ) demonstrates the evaporation effect between Spray G3 and Spray G3 Cold.

yielded by different models may lie in the droplet momentum due to large droplets generated by the blob method. It merits a more in-depth investigation by extracting the Weber number (We) and the Ohnesorge number (Oh).

Fig. 16 presents a comparison of different droplets' distribution within the breakup regime at  $a\text{SOI} = 0.58$  ms. In comparison to the spray shape using the statistic droplet distribution method, as shown in Fig. 10(a), the sharp plume tips appear in the Lagrangian fields, as shown in Fig. 16(a). Using the Blob method, the ejected Lagrangian parcels are at the size of the inner-nozzle diameter (165  $\mu\text{m}$ ). Although the same momentum setup is applied from the injection model, the Weber number of the droplets in the vicinity of the nozzle exit is higher, and the vast majority of the droplets still lie on the shear breakup regime, as shown in Fig. 16(b). In the spray downstream region, the majority of the droplets are still at the multi-mode and bag breakup regime stages, in contrast, with the droplets using the droplet distribution function. Thus, it is evident using the blob method that the liquid droplets experience a delayed breakup, resulting in sharp spray plume tips downstream.

Regardless of which droplet distribution models are utilized, the obtained momentum must be conserved using the same injection model.

Using the blob method, the Lagrangian parcels may contain lower-density liquid fuel. This phenomenon can be proven by comparing the cross-section liquid volume fraction (LVF) using 3-D computer tomographic reconstruction, as shown in Figs. 5 and 6.

Fig. 17 compares the liquid volume fraction (LVF) at a cross-section  $z = 30$  mm, which is recommended by ECN. According to the experimental data, the spray penetrates the cross-section in the shape of a complete circle. The spray does not disperse, although there are some weak signals in the surroundings. This phenomenon can be reproduced in Case 1 using the statistical droplet distribution method. In contrast, the spray is notably dispersed in Case 2 using the blob method. The results reflect the fact that using the blob method with the same mass and velocity setup for the injection model, the Lagrangian parcels may contain lower-density liquid fuel. Fig. 18 further compares the averaged LVF profiles of the eight plumes and the location of the plume center obtained from 3-D computer tomographic reconstruction. This makes it possible to quantitatively investigate the LVF signal produced by different simulations. Case 1, using the statistical droplet distribution method, yields a concentrated LVF signal and a narrower profile than experimental data, although the plume cross-section shapes are consistent with experimental data. On the other hand, Case 2, using the blob method, yields a dispersed LVF signal. This results in a mismatch with the plume center acquired by 3-D computer tomographic reconstruction, as shown in Fig. 18(b).

Utilizing the blob method as an injection distribution model is a practical approach to achieving accurate penetration lengths. However, its application can introduce uncertainties, especially when dealing with different types of injectors, and it tends to overpredict the size of ejected Lagrangian parcels, particularly in the case of ECN Spray G. This overprediction leads to unphysical spray plume tips downstream due to the delayed breakup process. Additionally, the larger Lagrangian parcels result in smaller densities, thereby generating a dispersed liquid volume fraction (LVF).

#### 4.2. Late-injection condition (Spray G1)

In the previous section, the proposed CFD framework has been proven capable of capturing the spray penetration and spray plume

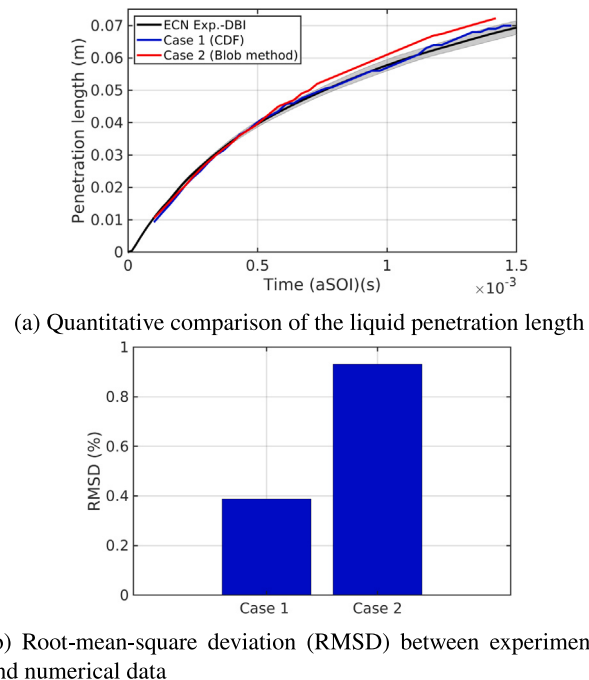


Fig. 15. Comparison between different droplet distribution models in liquid phase.

boundary in both the liquid and vapor phases under early-injection conditions. However, GDI engines operate not only under early-injection conditions (to achieve homogeneous combustion) but also under late-injection conditions (for stratified combustion). The latter type of combustion takes place during the compression phase and close to the cylinder top dead center (TDC) [57]. There is limited time for spray atomization and further mixture with the in-cylinder flow to achieve lean or ultra-lean stratified combustion. The Engine Combustion Network (ECN) thus set up engine-like late-injection operating conditions to acquire an in-depth understanding. The operating conditions of Spray G1 are shown in Fig. 4 and Table 1.

Fig. 19 provides a quantitative and qualitative comparison in the liquid phase using the projected liquid volume (PLV) data. A simulation conducted by a research group in ECN using LES and their Corrected Distortion model [31] are utilized for this comparison, as shown in Table 2 [49]. The comparison is referred to as Case 6 in Fig. 19(a). Unlike early-injection cases, (Spray G3 and Spray G3 Cold), Spray G1 yields strong evaporation, and consequently, the extinction of the projected liquid volume (PLV) signal takes place at approximately aSOI = 1.1 ms. This phenomenon is captured in Case 4. On the contrary, PLV extinction remains absent in Cases 5 and 6, which use the blob method as an injection distribution model. Furthermore, the liquid

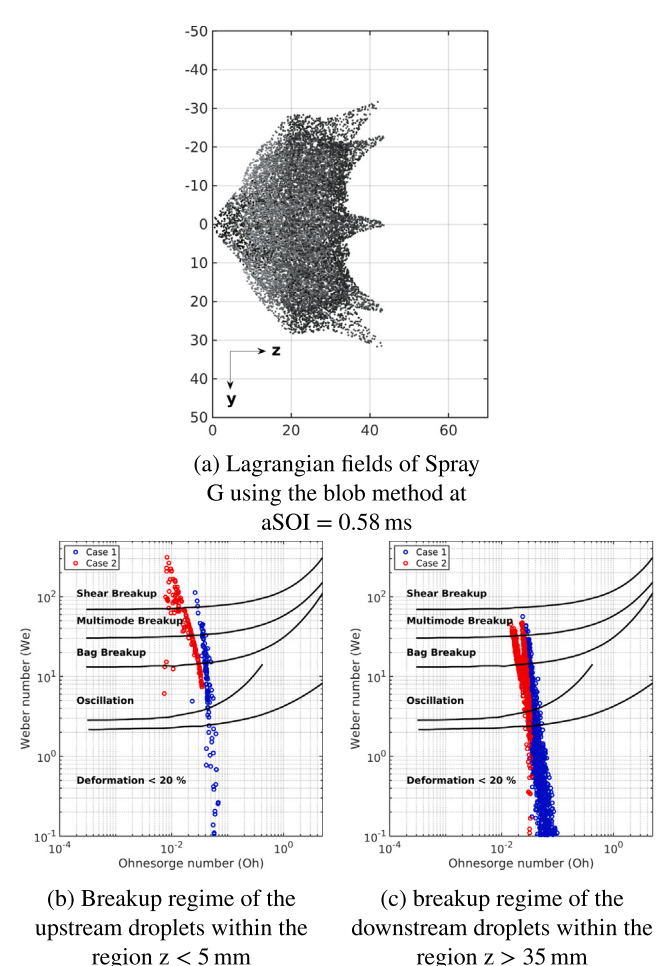


Fig. 16. Comparison of the spray droplets distribution under G3 condition within the breakup regime diagram by Hsiang and Faeth [37].

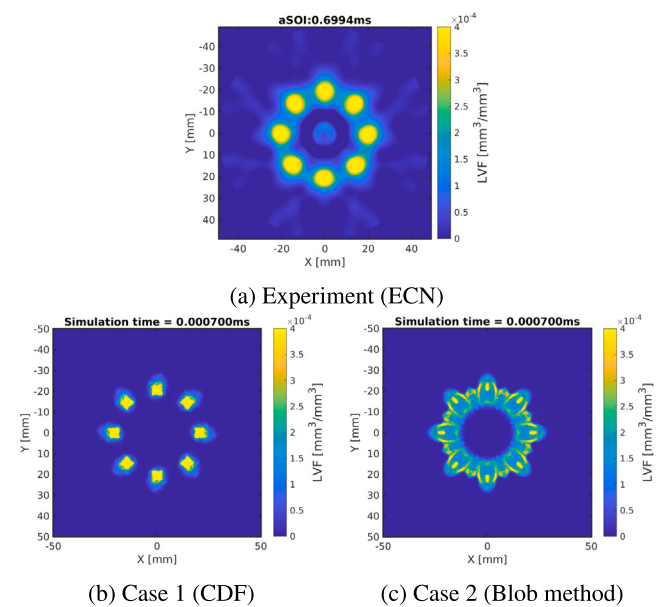
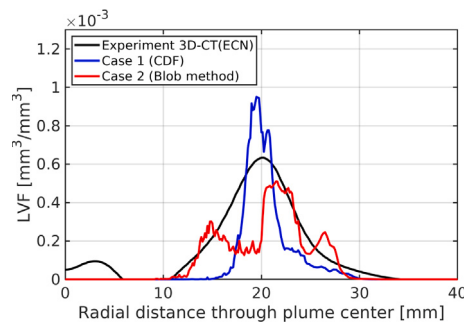
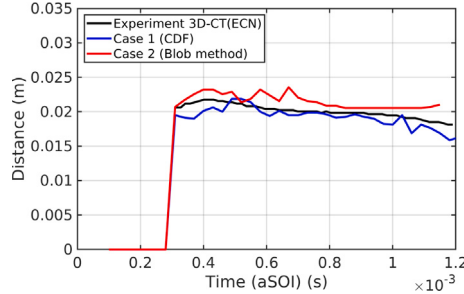


Fig. 17. Comparison of the liquid volume fraction (LVF) at cross-section z = 30 mm acquired by 3-D computer tomographic reconstruction.



(a) The averaged LVF profiles of the eight plumes



(b) The location of the plume center

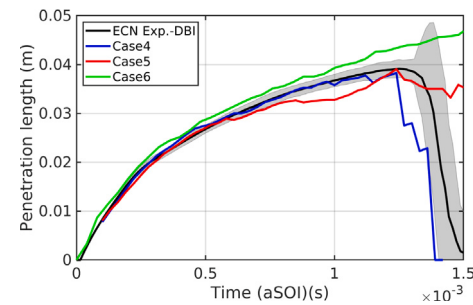
**Fig. 18.** Quantitative comparison of the liquid volume fraction (LVF) at cross-section  $z = 30$  mm acquired by 3-D computer tomographic reconstruction.

penetration of Spray G1 is shorter than in early-injection cases due to the high ambient pressure and temperature.

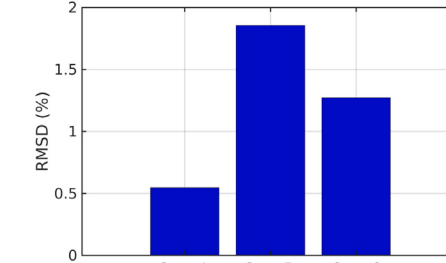
By employing the identical RMSD methodology up to  $aSOI = 1.5$  ms, as detailed in Section 4.1.2, it becomes evident that Case 4, adept at capturing the pronounced evaporation phenomenon, shows the most minimal divergence of 0.5% from the experimental dataset, as illustrated in Fig. 19(b). In stark contrast, Case 5 and Case 6 exhibit divergences of roughly 2% and 1.3% from the experimental dataset, respectively. They are three and two times greater than that of Case 4.

Fig. 19(c) presents a qualitative comparison of the projected liquid volume (PLV) boundary, contrasting the experimental data and numerical results. The blue and red solid lines refer to Cases 4 and 5, respectively. In Case 5, the sharp tips of the spray downstream disappear compared with the Spray G3 case. Compared to early-injection conditions, Spray G1 has a more compact plume shape due to high ambient pressure and temperature. Both experimental and numerical data show that the projected liquid boundary starts to become extinct at  $aSOI = 1.12$  ms. The extinction of the projected liquid boundary is almost complete at  $aSOI = 1.21$  ms. It results in a sudden drop in the liquid penetration length at  $aSOI = 1.25$  ms, as shown in Fig. 19(a). In Fig. 19(b), Case 4, using the statistical droplet distribution method, behaves consistently with the experimental data. Interestingly, Case 5 has slower extinction, and the projected liquid volume (PLV) boundary remains intact even at  $aSOI = 1.25$  ms. Furthermore, the extinction in Case 5 starts from the edge instead of in the middle, as the experimental data and the data in Case 4. This phenomenon likely occurs due to the size of the liquid droplets. As the Lagrangian parcels introduced to the constant-volume chamber in Case 5 are of the size as the inner-injector diameter ( $165 \mu\text{m}$ ), the volume-to-surface ratio of each droplet is much larger than the real liquid droplets. It can yield an evaporation delay, resulting in the phenomenon shown in Fig. 19.

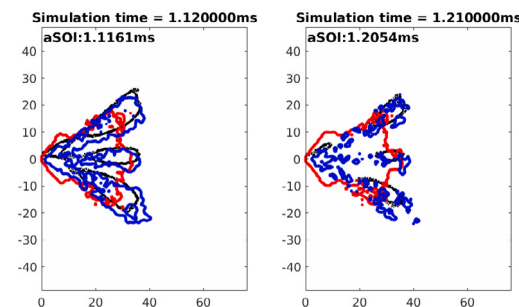
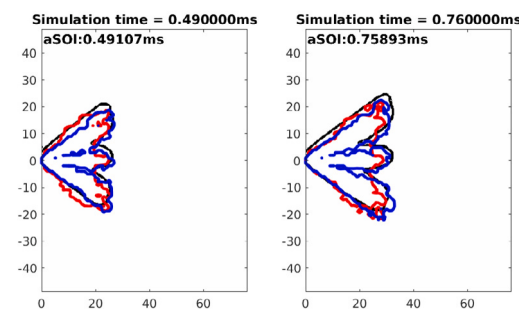
Fig. 20 further demonstrates the time evolution of the Sauter mean diameter (SMD). The measured section is at  $z = 15$  mm. The experimental SMD data is acquired from ECN and measured by means of phase-Doppler interferometry (PDI) [9,13]. It is worth noting that



(a) Quantitative comparison of the liquid penetration length



(b) RMSD between experimental and numerical data



(c) Qualitative comparison of the projected liquid plume boundary derived from projected liquid volume (PLV) data (Note: black line: experiment, blue line: Case 4 and red line: Case 5)

**Fig. 19.** A comparison of different simulations in the liquid phase. (For interpretation of the references to color in this figure legend, the reader is referred to the web version of this article.)

the measured experimental data is focused on a single spray plume, whereas the numerical data is averaged from eight spray plumes. The experimental droplet SMD lies in a region between 7 to 10  $\mu\text{m}$  after  $aSOI = 0.9$  ms, whereas the numerical droplet SMD in Case 4 is approximately at 7  $\mu\text{m}$ . Although this is a slight underprediction, Case 4 agrees well with the measured SMD data. Interestingly, the numerical droplet's

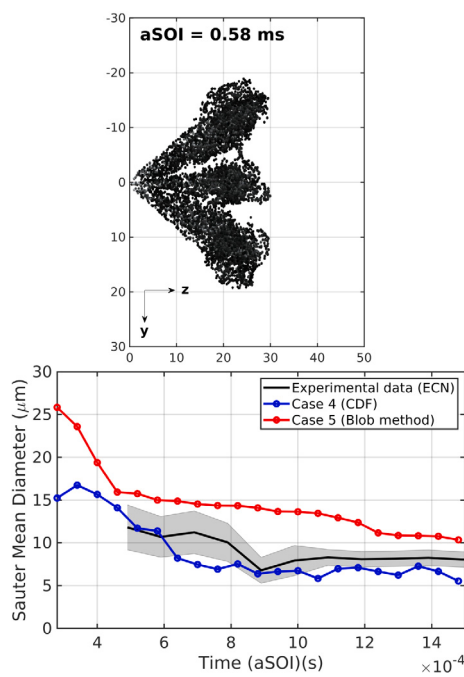


**Fig. 20.** Sauter mean diameter (SMD) time evolution profile at section  $z = 15$  mm; the experimental data is measured by Scott Parish (GM) using phase-doppler interferometry (PDI) [9,13]. (Note: The PDI data is temporal and spatial with a radial direction. The black solid line is the spatially averaged data, and the shadow represents the range.)

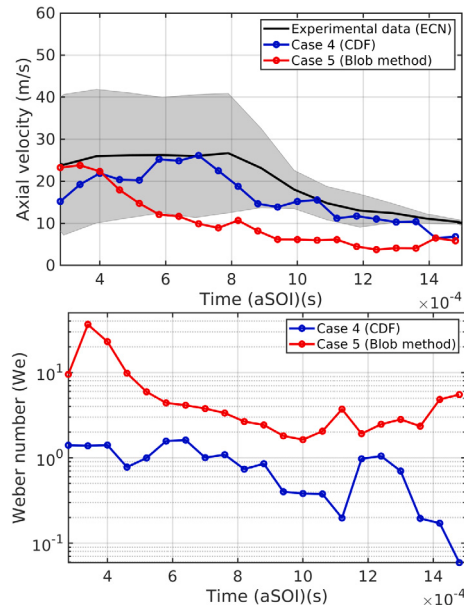


**Fig. 21.** Mean velocity normal to the  $z$  direction profile and the corresponding mean Weber number profile with time at section  $z = 15$  mm; the experimental data is measured by Scott Parish (GM) using phase-Doppler interferometry (PDI) (ECN 3rd workshop) [9]. (Note: the PDI data is temporal and spatial with a radial direction. The black solid line is the spatially averaged data, and the shadow represents the range.)

SMD in Case 5 lies in the range between 12.5 to 16  $\mu\text{m}$  after  $\text{aSOI} = 0.9$  ms. It is 1.5 to 2 times larger than the measured liquid droplets' SMD. Large droplets can yield delayed evaporation, which explains the problem with signal extinction and liquid penetration length, as shown in Fig. 19.

So far, the delayed evaporation effect has been observed in the case using the blob method and is further investigated by comparing the Sauter mean diameter of the liquid droplets at the cross-section  $z = 15$  mm. The deviation in the liquid droplet size can further affect the momentum and inertial force of the droplets and, consequently, result in a different penetration length. It merits more investigation by extracting the axial velocity of the plume (normal to the  $z$ -direction) and its corresponding Weber number ( $\text{We}$ ) at the cross-section  $z = 15$  mm, as shown in Fig. 21.

The axial velocity in Case 4 agrees well with the experimental data, whereas the velocity in Case 5 decays notably after the injection  $\text{aSOI} = 0.78$  ms. This explains the underprediction of the liquid penetration length in Case 5 after  $\text{aSOI} = 0.78$  ms, as shown in Fig. 19. Case 5, using the blob method, has a relatively high Weber number, indicating a higher inertial force but a fast axial velocity decay. The high Weber number might be due to the droplet size. Furthermore, the Weber number in Case 4 strongly decays after  $\text{aSOI} = 1.25$  ms, whereas it remains in Case 5. This reflects the full evaporation of the liquid droplets. A phenomenon of this kind can be observed in Fig. 19 as liquid signal extinction.

Under late-injection conditions (Spray G1), evaporation effects are crucial in spray formation. Evaporation effects are susceptible to the accurate prediction of droplet size. Using the blob method, droplet size is overpredicted, resulting in an evaporation delay.

## 5. Conclusion

This study presents a comprehensive analysis and validation of suitable Lagrangian models using Large Eddy Simulation (LES) for a GDI spray within a hole-type injector, supported by extensive experimental data and a DNS inner-nozzle flow simulation. The theoretical approach and performance of the proposed suite of models have been extensively discussed. By considering droplet deformation, the proposed one effectively captures the intricate characteristics and details of ECN Spray G under both early- and late-injection conditions. The simulation results exhibit strong agreement with experimental data in terms of both qualitative and quantitative aspects.

Several noteworthy findings have emerged from this study:

1. The liquid spray, owing to the counter-bore configuration, undergoes primary atomization within the inner-nozzle region, with complete liquid core breakup occurring in the vicinity of the nozzle exit. A liquid breakup regime map reveals that the vast majority of the liquid droplets experience oscillation and deformation.
2. Evaporation effects are evident in the Spray G3 case, with 45% of the liquid mass remaining at the end of the injection duration. In contrast, the Spray G3 Cold case exhibits a significantly higher liquid mass retention of 85% at the end of the injection duration. Cases with minimal evaporation display a visible spray plume tip downstream, as observed in the Spray G3 Cold case.
3. The blob method, used as the droplet distribution model, yields satisfactory results in comparisons of global quantities, such as the penetration length in both the liquid and vapor phases. However, assuming that the ejected Lagrangian parcels have the size of the injector's inner diameter can lead to delays in droplet breakup and the formation of unphysically sharp spray plume tips in the Spray G3 case. Furthermore, it results in a more dispersed liquid volume fraction (LVF) compared to experimental data.
4. Under late-injection conditions with high ambient pressure and temperature (Spray G1), the spray has a more compact plume shape and penetrates less compared with cases under early-injection conditions. Due to high evaporation in the Spray G1 case, the liquid spray signal extinction can be captured in the proposed CFD framework. However, using the blob method, the

liquid droplets have a strong evaporation delay, and the liquid spray signal does not disappear. This phenomenon appears in simulations by both the author and ECN. A statistical droplet distribution function is highly recommended for ECN Spray G and all injectors feature a counter-bore configuration.

The proposed suite of models using Large Eddy Simulation (LES) proves capable of capturing spray formations and their characteristics under engine-like conditions. Building upon this promising start, it can be further applied to spray-wall interaction or spray-flow interaction within GDI engines. Both play a crucial role in the air-fuel mixture, consequently influencing the performance of combustion and even soot formations. The next step will be to use the proposed CFD framework to investigate spray formation and spray-flow interaction within a GDI engine flow bench under early-injection conditions.

#### CRediT authorship contribution statement

**Hao-Pin Lien:** Writing – review & editing, Writing – original draft, Visualization, Validation, Resources, Methodology, Investigation, Formal analysis, Data curation, Conceptualization. **Yongxiang Li:** Writing – review & editing, Visualization, Methodology, Data curation, Conceptualization. **Andrea Pati:** Writing – review & editing, Supervision, Data curation. **Amsini Sadiki:** Writing – review & editing, Supervision, Data curation. **Christian Hasse:** Writing – review & editing, Supervision, Funding acquisition, Data curation.

#### Declaration of competing interest

The authors declare that they have no known competing financial interests or personal relationships that could have appeared to influence the work reported in this paper.

#### Data availability

Data will be made available on request.

#### Acknowledgments

The authors gratefully acknowledge the computing time provided to them at the NHR Center NHR4CES at TU Darmstadt (project number P002035). This is funded by the Federal Ministry of Education and Research, and the state governments participating on the basis of the resolutions of the GWK for national high-performance computing at universities ([www.nhr-verein.de/unsere-partner](http://www.nhr-verein.de/unsere-partner)). The research work was funded by the Deutsche Forschungsgemeinschaft (DFG, German Research Foundation), project number 237267381 (TRR 150), and the Darmstadt Graduate School of Energy Science and Engineering. Additionally, the authors extend their heartfelt appreciation to Engine Combustion Network (ECN) for granting access to the experimental data used in this study. Special thanks are also extended to Dr. Lyle Pickett and Dr. Tuan Nguyen for their valuable contributions and fruitful discussions throughout the research process.

#### Appendix A

As the study utilizes Large Eddy Simulation (LES), the mesh quality affects the resolution of the turbulence. Celik et al. [56] developed three different indexes based on the principle of the turbulence-resolved scale from [58]. According to Celik et al. [56], a sufficient Large Eddy Simulation (LES) is suggested to contain 75 to 85% of the kinetic energy. The three indexes, which are based on the turbulent viscosity, dissipation, and kinetic energy, thus focus on different examined parameters depending on the type of the sub-grid model used in Large Eddy Simulation (LES). The study employs the sigma model developed by Nicoud et al. [38]. This is an algebraic eddy viscosity model in

which the eddy viscosity  $\nu_t$  is directly solved, unlike the one-equation model [59]. Therefore, the corresponding examining index ( $IQ_{LES,v}$ ) is written as:

$$IQ_{LES,v} = \frac{1}{1 + \alpha_v (\frac{\nu_{t,eff}}{\nu})^n}, \quad (38)$$

where  $\alpha_v$  is a constant with a value of 0.05 and  $n = 0.53$ . The effective viscosity ( $\nu_{t,eff}$ ) is the sum of the molecular viscosity ( $\nu$ ) and the eddy viscosity ( $\nu_t$ ). Fig. 22 shows the highlighted region ( $Y = -20$  mm to  $Y = 20$  mm and  $Z = 0$  mm to  $Z = 40$  mm) of the spray velocity and the quality examining index.

In Fig. 22(b), the viscosity ratio ( $\frac{\nu_{t,eff}}{\nu}$ ) is employed to weigh the overall viscosity against the molecular viscosity. The ratio reaches unity as the sub-grid model produces no sub-grid viscosity. As per Celik et al. [56], the ratio ought to be less than 20 to settle 80% of the kinetic energy. Therefore, the mesh quality presented is adequate with a global viscosity ratio ranging from 15 to 20, corresponding to an index ( $IQ_{LES,v}$ ) value of around 80% to 85%. Although the maximum viscosity ratio value in the mesh transition region and the injector tip is 25.58, this corresponds to an examination index value of 78.205%, within the suggested range of 75% to 85% of the kinetic energy [56].

#### Appendix B. Acronyms

**LES** Large Eddy Simulation

**DNS** Direct Numerical Simulation

**RANS** Reynolds-averaged Navier Stokes

**aSOI** time after the start of injection

**DBIEI** diffused backlight illumination extinction imaging

**ICEs** internal combustion engines

**DISI** direct-injection spark-ignition

**SI** spark-ignition

**GDI** gasoline direct-injection

**PFI** port fuel injection

**ECN** Engine Combustion Network

**We** Weber number

**Oh** Ohnesorge number

**RMSD** Root-mean-square deviation

**CDF** cumulative distribution function

**PLV** projected liquid volume

**LVF** liquid volume fraction

**PDI** phase-Doppler interferometry

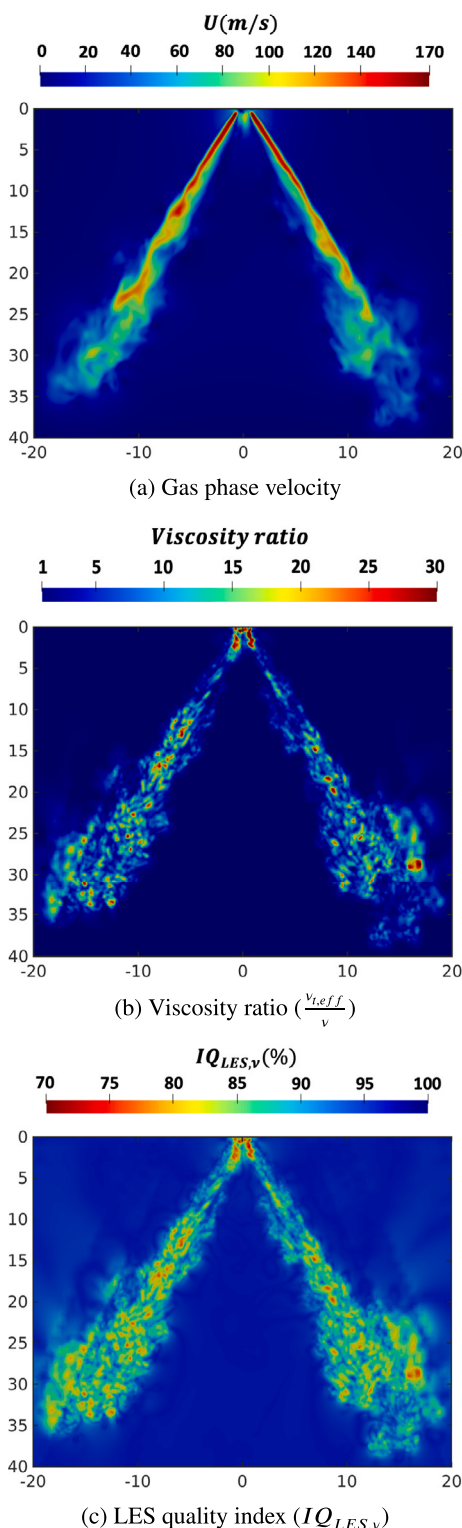


**Fig. 22.** Examining mesh quality at a time after the start of injection (aSOI) = 0.64 ms.

## References

- [1] EPA. The 2022 EPA automotive trends report. 2022.
- [2] Zhao H. Advanced direct injection combustion engine technologies and development. Woodhead publishing in mechanical engineering, CRC Press; 2010.
- [3] Zhao F, Lai MC, Harrington DL. Automotive spark-ignited direct-injection gasoline engines. Elsevier; 2000, OCLC: 437191525.
- [4] Mitroglou N, Nouri JM, Gavaises M, Arcoumanis C. Spray characteristics of a multi-hole injector for direct-injection gasoline engines. *Int J Engine Res* 2006;7(3):255–70. <http://dx.doi.org/10.1243/146808705X62922>, 2041-3149. URL <http://journals.sagepub.com/doi/10.1243/146808705X62922>.
- [5] Mitroglou N, Nouri JM, Yan Y, Gavaises M, Arcoumanis C. Spray structure generated by multi-hole injectors for gasoline direct-injection engines. 2007, p. 2007-01-1417. <http://dx.doi.org/10.4271/2007-01-1417>, URL <https://www.sae.org/content/2007-01-1417/>.
- [6] Sick V, Drake MC, Fansler TD. High-speed imaging for direct-injection gasoline engine research and development. *Exp Fluids* 2010;49(4):937–47. <http://dx.doi.org/10.1007/s00348-010-0891-3>, 1432-1114. URL <http://link.springer.com/10.1007/s00348-010-0891-3>.
- [7] Hoffmann G, Befrui B, Berndorfer A, Piock WF, Varble DL. Fuel system pressure increase for enhanced performance of GDI multi-hole injection systems. *SAE Int J Engines* 2014;7(1):519–27. <http://dx.doi.org/10.4271/2014-01-1209>, URL <https://www.sae.org/content/2014-01-1209/>.
- [8] Saha K, Quan S, Battistoni M, Som S, Senecal PK, Pomraning E. Coupled Eulerian internal nozzle flow and Lagrangian spray simulations for GDI systems. 2017, p. 2017-01-0834. <http://dx.doi.org/10.4271/2017-01-0834>, URL <https://www.sae.org/content/2017-01-0834/>.
- [9] ECN Spray G data. 2023, URL <https://ecn.sandia.gov/data/sandia-spray-g-data/>.
- [10] Hwang J, Weiss L, Karathanassis IK, Koukouvinis P, Pickett LM, Skeen SA. Spatio-temporal identification of plume dynamics by 3D computed tomography using engine combustion network spray G injector and various fuels. *Fuel* 2020;280:118359. <http://dx.doi.org/10.1016/j.fuel.2020.118359>, URL <https://linkinghub.elsevier.com/retrieve/pii/S0016236120313557>.
- [11] Duke DJ, Swantek AB, Sovis NM, Tilocco FZ, Powell CF, Kastengren AL, Gürsoy D, Bicer T. Time-resolved X-ray tomography of gasoline direct injection sprays. *SAE Int J Engines* 2015;9(1):143–53. <http://dx.doi.org/10.4271/2015-01-1873>, URL [https://www.sae.org/content/2015-01-1873/](https://www.sae.org/content/2015-01-1873).
- [12] Duke DJ, Kastengren AL, Matusik KE, Swantek AB, Powell CF, Payri R, Viquerizo D, Itani L, Bruneaux G, Grover RO, Parrish S, Markle L, Schmidt D, Manin J, Skeen SA, Pickett LM. Internal and near nozzle measurements of Engine Combustion Network “Spray G” gasoline direct injectors. *Exp Therm Fluid Sci* 2017;88:608–21. <http://dx.doi.org/10.1016/j.expthermflusci.2017.07.015>, URL <https://linkinghub.elsevier.com/retrieve/pii/S089417771730211X>.
- [13] Weiss L, Wensing M, Hwang J, Pickett LM, Skeen SA. Development of limited-view tomography for measurement of Spray G plume direction and liquid volume fraction. *Exp Fluids* 2020;61(2):51. <http://dx.doi.org/10.1007/s00348-020-2885-0>, 1432-1114. URL <http://link.springer.com/10.1007/s00348-020-2885-0>.
- [14] Tryggvason G, Scardovelli R, Zaleski S. Direct numerical simulations of gas-liquid multiphase flows. Cambridge University Press; 2011, <http://dx.doi.org/10.1017/CBO9780511975264>.
- [15] Yue Z, Battistoni M, Som S. Spray characterization for engine combustion network Spray G injector using high-fidelity simulation with detailed injector geometry. 2020.
- [16] Arienti M, Wenzel E. Detailed evaporation modelling for gasoline direct injection: iso-octane vs. E30. 2022.
- [17] Navarro-Martinez S, Tretola G, Yosri MR, Gordon RL, Vogiatzaki K. An investigation on the impact of small-scale models in gasoline direct injection sprays (ECN Spray G). *Int J Engine Res* 2020;21(1):217–25. <http://dx.doi.org/10.1177/1468087419889449>, 2041-3149. URL <http://journals.sagepub.com/doi/10.1177/1468087419889449>.
- [18] Tretola G, Vogiatzaki K, Navarro-Martinez S. Implementation of a probabilistic surface density volume of fluid approach for spray atomisation. *Comput & Fluids* 2021;230:105121. <http://dx.doi.org/10.1016/j.compfluid.2021.105121>, URL <https://www.sciencedirect.com/science/article/pii/S0045793021002668>.
- [19] Tretola G, Navarro-Martinez S, Vogiatzaki K. Primary break-up characterisation and droplet statistics of multi-hole sprays using a probabilistic surface density methodology. 2022.
- [20] Befrui B, Aye A, Bossi A, Markle LE, Varble DL. ECN GDI Spray G: Coupled LES jet primary breakup - Lagrangian spray simulation and comparison with data. 2016.
- [21] Paredi D, Lucchini T, D'Errico G, Onorati A, Montanaro A, Allocca L, Ianniello R. Combined experimental and numerical investigation of the ECN Spray G under different engine-like conditions. 2018, p. 2018-01-0281. <http://dx.doi.org/10.4271/2018-01-0281>, URL <https://www.sae.org/content/2018-01-0281/>.
- [22] Duronio F, Di Mascio A, Villante C, Anatone M, De Vita A. ECN Spray G: Coupled Eulerian internal nozzle flow and Lagrangian spray simulation in flash boiling conditions. *Int J Engine Res* 2022-04-05;14680874221090732, 2041-3149. URL <http://dx.doi.org/10.1177/14680874221090732>.
- [23] Payri R, Marti-Aldaravi P, Abboud R, Bautista A. Numerical analysis of GDI flash boiling sprays using different fuels. *Energies* 2021-09-18;14(18):5925. <http://dx.doi.org/10.3390/en14185925>, URL <https://www.mdpi.com/1996-1073/14/18/5925>.

- [24] Geschwindner C, Kranz P, Welch C, Schmidt M, Böhm B, Kaiser SA, De la Morena J. Analysis of the interaction of Spray G and in-cylinder flow in two optical engines for late gasoline direct injection. *Int J Engine Res* 2020;21(1):169–84. <http://dx.doi.org/10.1177/1468087419881535>, 2041-3149. URL <http://journals.sagepub.com/doi/10.1177/1468087419881535>.
- [25] Pati A, Paredi D, Welch C, Schmidt M, Geschwindner C, Böhm B, Lucchini T, D'Errico G, Hasse C. Numerical and experimental investigations of the early injection process of Spray G in a constant volume chamber and an optically accessible DISI engine. *Int J Engine Res* 2022;23(12):2073–93. <http://dx.doi.org/10.1177/14680874211039422>, 2041-3149. URL <http://journals.sagepub.com/doi/10.1177/14680874211039422>.
- [26] Tagliante F, Nguyen TM, Pickett LM, Sim HS. Large-eddy simulation of laser-ignited direct injection gasoline spray for emission control. *Energies* 2021;14(21):7276. <http://dx.doi.org/10.3390/en14217276>, URL <https://www.mdpi.com/1996-1073/14/21/7276>.
- [27] Luo K, Desjardins O, Pitsch H. DNS of droplet evaporation and combustion in a swirling combustor. 2008.
- [28] Hinrichs J, Schlotte K, Ibach M, Pitsch H, Weigand B. Modelling of the transport mechanisms in the direct neighbourhood of evaporating fuel droplets. 2020.
- [29] Amsden AA, O'Rourke PJ, Butler TD. KIVA-II: A computer program for chemically reactive flows with sprays. 1989. <http://dx.doi.org/10.2172/6228444>, URL <https://www.osti.gov/biblio/6228444>.
- [30] Crua C, Manin J, Pickett LM. On the transcrirical mixing of fuels at diesel engine conditions. *Fuel* 2017;208:535–48. <http://dx.doi.org/10.1016/j.fuel.2017.06.091>, URL <https://linkinghub.elsevier.com/retrieve/pii/S0016236117308013>.
- [31] Nguyen TM, Dahms RN, Pickett LM, Tagliante F. The Corrected Distortion model for Lagrangian spray simulation of transcrirical fuel injection. *Int J Multiph Flow* 2022;148:103927. <http://dx.doi.org/10.1016/j.ijmultiphaseflow.2021.103927>, URL <https://linkinghub.elsevier.com/retrieve/pii/S0301932221003311>.
- [32] Amsden AA, O'Rourke PJ, Butler TD. KIVA-II: A computer program for chemically reactive flows with sprays. 1989, URL <http://www.osti.gov/servlets/purl/6228444/>.
- [33] Liu AB, Mather D, Reitz RD. Modeling the effects of drop drag and breakup on fuel sprays. 1993, 930072. <http://dx.doi.org/10.4271/930072>, URL <https://www.sae.org/content/930072>.
- [34] Taylor G, Establishment GBCDE. The shape and acceleration of a drop in a high speed air stream. 1974, URL <https://books.google.de/books?id=veHJzQEACAAJ>.
- [35] Patterson MA, Reitz RD. Modeling the effects of fuel spray characteristics on diesel engine combustion and emission. *SAE Trans* 1998;107:27–43, 25771531. URL <http://www.jstor.org/stable/44736506>.
- [36] Dahms RN, Oefelein JC. The significance of drop non-sphericity in sprays. *Int J Multiph Flow* 2016;86:67–85. <http://dx.doi.org/10.1016/j.ijmultiphaseflow.2016.07.010>, URL <https://linkinghub.elsevier.com/retrieve/pii/S030193221530104X>.
- [37] Hsiang L-P, Faeth G. Drop deformation and breakup due to shock wave and steady disturbances. *Int J Multiph Flow* 1995;21(4):545–60. [http://dx.doi.org/10.1016/0301-9322\(94\)00095-2](http://dx.doi.org/10.1016/0301-9322(94)00095-2), URL <https://linkinghub.elsevier.com/retrieve/pii/0301932294000952>.
- [38] Nicoud F, Toda HB, Cabrit O, Bose S, Lee J. Using singular values to build a subgrid-scale model for large eddy simulations. *Phys Fluids* 2011;23(8). <http://dx.doi.org/10.1063/1.3623274>.
- [39] Haider A, Levenspiel O. Drag coefficient and terminal velocity of spherical and nonspherical particles. *Powder Technol* 1989;58(1):63–70. [http://dx.doi.org/10.1016/0032-5910\(89\)80008-7](http://dx.doi.org/10.1016/0032-5910(89)80008-7), URL <https://linkinghub.elsevier.com/retrieve/pii/0032591089800087>.
- [40] O'Rourke PJ, Amsden AA. The tab method for numerical calculation of spray droplet breakup. 1987, 872089. <http://dx.doi.org/10.4271/872089>, URL <https://www.sae.org/content/872089>.
- [41] Richter A, Nikrityuk PA. Drag forces and heat transfer coefficients for spherical, cuboidal and ellipsoidal particles in cross flow at sub-critical Reynolds numbers. *Int J Heat Mass Transfer* 2012;55(4):1343–54. <http://dx.doi.org/10.1016/j.ijheatmasstransfer.2011.09.005>, URL <https://linkinghub.elsevier.com/retrieve/pii/S0017931011005023>.
- [42] Feng Z-G, Michaelides EE. Drag coefficients of viscous spheres at intermediate and high Reynolds numbers. *J Fluids Eng* 2001;123(4):841–9. <http://dx.doi.org/10.1115/1.1412458>, 1528-901X. URL <https://asmedigitalcollection.asme.org/fluidsengineering/article/123/4/841/459295/Drag-Coefficients-of-Viscous-Spheres-at>.
- [43] Feng Z-G, Michaelides EE. Heat and mass transfer coefficients of viscous spheres. *Int J Heat Mass Transfer* 2001;44(23):4445–54. [http://dx.doi.org/10.1016/S0017-9310\(01\)00090-4](http://dx.doi.org/10.1016/S0017-9310(01)00090-4), URL <https://linkinghub.elsevier.com/retrieve/pii/S0017931001000904>.
- [44] Miller R, Harstad K, Bellan J. Evaluation of equilibrium and non-equilibrium evaporation models for many-droplet gas-liquid flow simulations. *Int J Multiph Flow* 1998;24(6):1025–55. [http://dx.doi.org/10.1016/S0301-9322\(98\)00028-7](http://dx.doi.org/10.1016/S0301-9322(98)00028-7), URL <https://linkinghub.elsevier.com/retrieve/pii/S0301932298000287>.
- [45] Bellan J, Summerfield M. Theoretical examination of assumptions commonly used for the gas phase surrounding a burning droplet. *Combust Flame* 1978;33:107–22. [http://dx.doi.org/10.1016/0010-2180\(78\)90054-8](http://dx.doi.org/10.1016/0010-2180(78)90054-8), URL <https://linkinghub.elsevier.com/retrieve/pii/0010218078900548>.
- [46] Nagaoka M, Kawamura K. A deforming droplet model for fuel spray in direct-injection gasoline engines. 2001, p. 2001-01-1225. <http://dx.doi.org/10.4271/2001-01-1225>, URL <https://www.sae.org/content/2001-01-1225>.
- [47] Pilch M, Erdman C. Use of breakup time data and velocity history data to predict the maximum size of stable fragments for acceleration-induced breakup of a liquid drop. *Int J Multiph Flow* 1987;13(6):741–57. [http://dx.doi.org/10.1016/0301-9322\(87\)90063-2](http://dx.doi.org/10.1016/0301-9322(87)90063-2), URL <https://linkinghub.elsevier.com/retrieve/pii/0301932287900632>.
- [48] Reitz RD, Diwakar R. Structure of high-pressure fuel sprays. 1987, 870598. <http://dx.doi.org/10.4271/870598>, URL <https://www.sae.org/content/870598>.
- [49] CFD data search. 2023, URL <https://ecn.sandia.gov/cfd-data-search/>.
- [50] Li Y, Ries F, Nishad K, Sun Y, Sadiki A. Direct numerical simulation of atomization characteristics of ECN Spray-G injector: In-nozzle fluid flow and breakup processes. *Fuel* 2023.
- [51] Bornschlegel S, Conrad C, Eichhorn L, Wensing M. Flashboiling atomization in nozzles for GDI engines. 2017, <http://dx.doi.org/10.4995/IJASS2017.2017.4750>.
- [52] Zuo B, Gomes AM, Rutland CJ. Modelling superheated fuel sprays and vaporization. *Int J Engine Res* 2000;1(4):321–36. <http://dx.doi.org/10.1243/1468087001545218>, 2041-3149. URL <http://journals.sagepub.com/doi/10.1243/1468087001545218>.
- [53] Bhatia B, De A. Flash boiling in sprays: Recent developments and modeling. *J Indian Inst Sci* 2019;99(1):93–104. <http://dx.doi.org/10.1007/s41745-019-0104-x>, 0019-4964. URL <http://link.springer.com/10.1007/s41745-019-0104-x>.
- [54] Pickett LM, Genzale CL, Manin J. Uncertainty quantification for liquid penetration of evaporating sprays at diesel-like conditions. *At Sprays* 2015;25(5):425–52. <http://dx.doi.org/10.1615/AtomizSpr.2015010618>, URL [http://www.dl.begellhouse.com/journals/6a7c7e10642258cc\\_441042be565b52ed\\_738986f63f3f0847.html](http://www.dl.begellhouse.com/journals/6a7c7e10642258cc_441042be565b52ed_738986f63f3f0847.html).
- [55] Westlys FR, Penney K, Ivarsson A, Pickett LM, Manin J, Skeen SA. Diffuse back-illumination setup for high temporally resolved extinction imaging. *Appl Opt* 2017;56(17):5028–38. <http://dx.doi.org/10.1364/AO.56.005028>, URL <https://opg.optica.org/ao/abstract.cfm?URI=ao-56-17-5028>.
- [56] Celik IB, Cehreli ZN, Yavuz I. Index of resolution quality for large eddy simulations. *J Fluids Eng* 2005;127(5):949–58. <http://dx.doi.org/10.1115/1.1990201>, 1528-901X. URL <https://asmedigitalcollection.asme.org/fluidsengineering/article/127/5/949/478030/Index-of-Resolution-Quality-for-Large-Eddy>.
- [57] Zhao H. Overview of gasoline direct injection engines. In: Advanced direct injection combustion engine technologies and development. Elsevier; 2010, p. 1–19. <http://dx.doi.org/10.1533/9781845697327.1>, URL <https://linkinghub.elsevier.com/retrieve/pii/B9781845693893500013>.
- [58] Pope SB. Turbulent flows. IOP Publishing; 2001.
- [59] Yoshizawa A, Horiuti K. A statistically-derived subgrid-scale kinetic energy model for the large-eddy simulation of turbulent flows. *J Phys Soc Japan* 1985;54(8):2834–9. <http://dx.doi.org/10.1143/JPSJ.54.2834>, 1347-4073. URL <http://journals.jps.jp/doi/10.1143/JPSJ.54.2834>.